MEASUREMENTS AND ASSESSMENT OF ADIABATIC FILM COOLING PERFORMANCE ON A GAS TURBINE VANE ENDWALL USING PSP TECHNIQUE

A Dissertation

by

MD. NAFIZ HOSSAIN KHAN CHOWDHURY

Submitted to the Office of Graduate and Professional Studies of
Texas A&M University
in partial fulfillment of the requirements for the degree of
DOCTOR OF PHILOSOPHY

Chair of Committee,	Je-Chin Han
Committee Members,	Gerald Morrison
	Hamn-Ching Chen
	Sai Lau
Head of Department,	Andreas A. Polycarpou

August 2017

Major Subject: Mechanical Engineering

ABSTRACT

Turbine vanes are typically assembled as a section containing single or double airfoil units in an annular pattern. First stage guide vane assembly results in two common mating interfaces - a gap between combustor and vane endwall while another from the adjacent sections, called slashface. High-pressure coolant could leak through these gaps to reduce the ingestion of hot gas and achieve certain cooling benefit. As vane endwall region flow field is already very complicated due to the presence of highly three-dimensional secondary flows, then a significant influence on endwall cooling can be expected due to the gap leakage flows. The entire study is divided into two parts. The first part of this dissertation investigates the endwall film cooling from gap leakage flows with the multiple rows of discrete film cooling holes inside the passages. The later part studies the film cooling performance of multiple endwall cooling designs including inlet leakage jet. Pressure Sensitive Paint (PSP) technique is used to obtain the detailed film cooling effectiveness distributions on the endwall of a scaled up mid-range industrial turbine vane geometry. Experiments are performed in a blow-down wind tunnel cascade facility at the isentropic exit Mach number of 0.5 corresponding to Reynolds number of 3.8×10^5 based on inlet conditions and axial chord length. Passive turbulence grid is used to generate freestream turbulence level about 19% with an integral length scale of 1.7 cm. The effect of coolant-to-mainstream mass flow ratio and density ratio on the film cooling have been studied. Results indicated that leakage coolants have significant influence on the endwall

film cooling and different endwall cooling designs are capable of achieving higher cooling effectiveness with relatively uniform coverage.

DEDICATION

This dissertation is lovingly dedicated to my parents, Mrs. Nazma Firoz and Late Chowdhury A. R. Khan Firoz. Their support, encouragement, and constant love have sustained me throughout my life.

ACKNOWLEDGEMENTS

I would like to thank the Texas A&M University, specifically the Mechanical Engineering department, for providing me the opportunity to receive a quality education. It is also my pleasure to acknowledge the people that have given me support and advice during my stay at the Texas A&M University.

First of all, I would like to give thanks to my supervisor, Dr. Je-chin Han for all his support, encouragement and critique that he has given me over the last five years. Dr. Han not only taught me a wealth of information but also provided every opportunity to achieve the goals that I had set out for myself. His invaluable guidance and perseverance have encouraged me to learn from my mistakes and move forward in my research. I would also like to thank Dr. Chen, Dr. Lau, and Dr. Morrison for giving their precious time to the advisory committee. I also want to extend my gratitude to Solar Turbines Inc., Samsung Techwin Inc., and Siemens Energy Inc. which supported my research throughout the Ph.D. program.

Second, I would like to thank all of my fellow Graduate students that I have worked with at TAMU including Chao-Cheng Shiau and Andrew Chen. These people were members of Turbine Heat Transfer Laboratory (THTL) Group. Having the privilege to

work with such a great and hands-on group of people made the last five years of my life a truly enjoyable experience. .

Third, I would like to thank Zahir from the aerospace machine shop for all his help in the fabrication and machining of my challenging designs and Ray Matthew for all his technical supports and suggestions during my stay at the Turbomachinery Laboratory. I am grateful to Sandy and Tandilyn for their administrative guidance with uncountable supports.

Finally, I would also like to thank my Mom, Nazma Firoz, for her never-ending unconditional love and continuous mental support she has given to me over the last years. Her prayer and love have helped me to endure tough times and remain focused on my thesis work. This degree would not be possible without her, and I will never be able to thank her enough. The support and dedication she shows to all her children are truly amazing. I would also like to thank the rest of my family including Dr. Zulkernine and Nadim for their constant support. Last but not the least, a very special friend, Kazi Rumy for standing beside me whenever I needed the help most. Thank you for being a wonderful family.

CONTRIBUTORS AND FUNDING SOURCES

Contributors

This work was supported by a dissertation committee consisting of Professor Je-Chin Han, Gerald Morrison and Sai Lau of the Department of Mechanical Engineering and Professor Hamn-Ching Chen of the Department of Civil Engineering.

All the work conducted for the dissertation was completed by the student independently.

Funding Sources

This work was made possible in part by Solar Turbines Inc. under Grant Number 32525-A847A and 405220-00001.

NOMENCLATURE

SYMBOLS

C	Chord length [cm]/Concentration
$\bar{C}_d$	Average discharge coefficient [-]
b	Bar width [cm]
D	Film cooling hole diameter [cm]
DR	Coolant-to-mainstream density ratio ($=\rho_c/\rho_m$)
L	Hole length [cm]
LE	Leading Edge [-]
MFR	Coolant-to-mainstream mass flow ratio [%]
M	Blowing ratio ($=\rho_c V_c/\rho_m V_m$) [-]
Ma	Mach number [-]
N/n	Row numbers/sample size
P	Pressure, Pitch [Pa, cm]
R	Recovery factor ($=\sqrt[3]{Pr}$)/Resistance
R_E	Autocorrelation coefficient [-]

S	Span [cm]
T	Temperature [K]/Period
TE	Trailing Edge [-]
Tu	Turbulence level [%]
$\overline{u}$	Mean velocity [m/s]
u'	Velocity fluctuation [m/s]
W	Molecular weight [gm]
$X/Y/Z$	Streamwise/Pitchwise/Pitchwise direction [-]

GREEK SYMBOLS

ρ	Density [kg/m^3]
γ	Heat capacity ratio [-]
Λ_x	Integral turbulence length scale [cm]
η_{ave}	Laterally averaged effectiveness [-]
μ	Mainstream viscosity [pa-s]
σ^2	Variance [m^4/s^4]
τ_E	Time scale [s]

SUBSCRIPTS

1	Streamwise direction
ax	Axial
ave	Average
aw	Adiabatic wall
blk	Black
c	Coolant
in	Inlet
ex	Exit
fg	Foreign Gas
m	Mainstream
o	Plenum/ambient
opt	Operational
o_2	Oxygen
ref	Reference
s	Static
t	Total

TABLE OF CONTENTS

Page

LIST OF FIGURES

Page

LIST OF TABLES

Page

CHAPTER I

INTRODUCTION

Gas turbine engines are widely used in land-based power generation and aero-propulsion applications due to higher fuel-to-power efficiency and lower emission. A gas turbine is an internal combustion engine that uses a high-temperature and high-pressure gas as the working fluid by transforming the thermal energy into mechanical energy. The required energy is produced from combustion of fuel with air resulting in the target temperatures in the turbine. In general, a gas turbine engine involves three major sections - compressor, combustion chamber, and turbine. The working fluid, from the combustor exit plane, is directed circumferentially by a set of guide vanes located at the downstream of the combustor nozzle to impinge upon turbine blades to extract the energy. Typically, a series of turbine blade rows are attached to a rotor/shaft assembly in multi-stages. For a land-based application, the shaft is coupled with the compressor side to bring the air into the gas turbine combustor and an electric generator to produce power as the shaft rotates. But in an aircraft engine, the shaft rotates the multi-stage compressors and a fan to draw more air into the combustion chamber and create thrust at the exit of the engine.

Gas turbine engines operate on a thermodynamic cycle called the Brayton cycle. Based on the thermal cycle analysis, there are two fundamental ways to increase the efficiency of the engine: increasing the compression ratio and increasing the turbine inlet temperature

(TIT). Apart from increasing high-pressure ratio, higher temperatures typically produce higher emission of NO_x. On the other hand, limiting the oxygen quantity to lower the NO_x emission leads to unacceptable high levels of CO and unburned carbon emissions. Thus, the challenge of achieving higher thermal efficiency for improved performance and less NO_x emissions is reflected in the fact that they are conflicting goals**.** However, this higher temperature is also limited by the yield point of the presently available turbine manufacturing material. Then, a major challenge of the gas turbine design is to develop effective cooling methods to reduce the heat loads toward turbine components so that higher TIT with better performance can be achieved. Some modern high-efficiency plants operate at firing temperatures more than 1600º C. The reason the components can withstand the extreme temperatures is due to the presence of a variety of cooling techniques [1]. External cooling, known as film cooling, and this technique is commonly used with various internal cooling methods to protect the turbine components from thermal failure. Most employed internal and external cooling methods are depicted in **Figure 1** for a typical cooling design in a turbine blade.

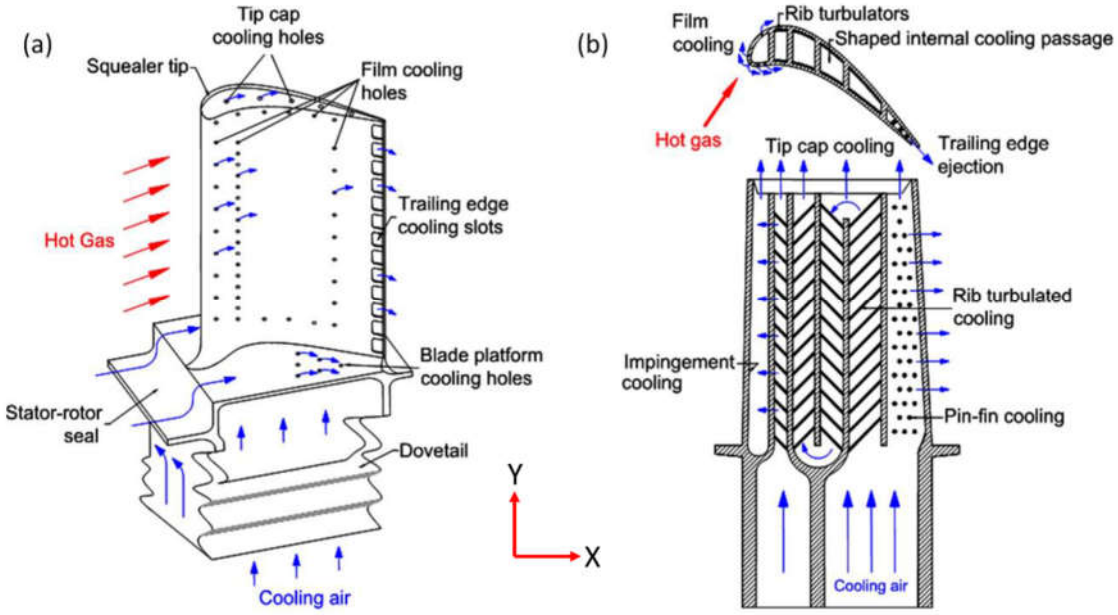

Figure 1 Typical gas turbine cooling techniques - a) external and b) internal

Recent endwall film cooling measurements have suggested the importance of leakage flow and reduction in the number of film cooling holes on endwall film cooling. A careful attention in positioning the cooling hole locations at critical areas of endwall including leakage flows can greatly reduce the hole numbers with improved cooling efficiency. This reduction in the number of holes can proportionally reduce the manufacturing cost. Current work is focused on the investigation of the endwall film cooling and documenting the effect of important parameters such as coolant-to-mainstream mass flow ratio (MFR) and density ratio (DR). These results should allow designers to improve predictive models and design more efficient and reliable gas turbine components.

CHAPTER II

LITERATURE SURVEY

The purpose of the research is to investigate the endwall film cooling under the engine representative flow situation. Since the gas turbines have been in operation for decades, numerous studies similar to this have been conducted in the past. A literature review of the major findings was conducted to assess the state of knowledge in the field and to add confidence to the experimental techniques.

The demand of higher Turbine Inlet Temperature (TIT) has risen steadily over the years for better performing engines, especially for land-based and propulsion applications. Meanwhile, engine manufacturers have developed advanced designs, which provide improved reliability. Part of this improved temperature capability is due to the migration toward enhanced component cooling schemes. Among all these schemes, first stage vane endwall cooling is the most critical part due to the presence of highly three-dimensional external flow field resulted from secondary flow interactions. Past studies also reveal that secondary flows not only augment the heat transfer between the mainstream gases and the uncooled endwall but also increase the aerodynamic loss in the cascade. Thus, to improve the endwall cooling design while dealing with the effects of these secondary flows, it is essential to have a clear understanding of the fundamental flow physics. Details of such flow physics are well documented in the literature by Langston et al. [2], Langston [3],

Sharma and Butler [4], Goldstein and Spores [5] and others. Furthermore, the introduction of leakage flow from the assembly gaps could make the flow field even more complicated. An overview of various leakage flows on the vane endwall is conceptually presented in **Figure 2**.

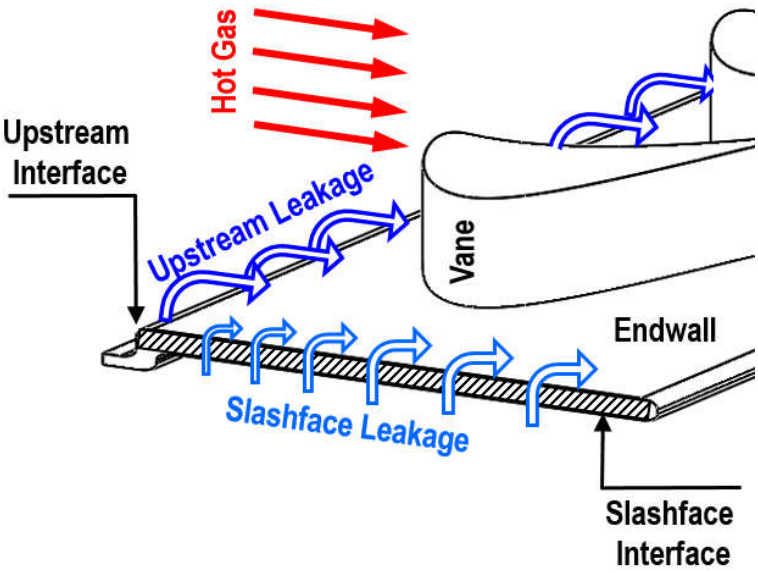

Figure 2 Conceptual view of leakage flows over the vane endwall

Typically, the vane endwall is cooled using film cooling technique. Takeishi et al. [6] investigated the film cooling through discrete film cooling (DFC) holes placed at the three different locations on a vane endwall. Their results showed that the coolant was swept from the pressure side of the passage toward the suction side. Also, the film cooling effectiveness near the leading edge (LE) of the suction side was very low due to the formation of the horseshoe vortex. Harasgama and Burton [7] placed film cooling holes

evenly along an iso-Mach line near the LE of passage but found that the pressure side of the passage received a very little coolant with this configuration. Similarly, Friedrichs et al. [8, 9] used ammonia and diazo technique to measure the amount of coolant coverage at every point on the endwall of a blade passage. They showed that evenly spaced rows of coolant holes did not provide even coverage for the endwall. The horseshoe vortex prevented the coolant from covering the LE of the blade, while the passage vortex lifted the coolant in its path off of the surface similar to the previous studies. The coolant in the passage was swept from the pressure side toward the suction side by the passage flow. Based on their findings, Friedrichs et al. [10] modified the film cooling hole locations with an attempt to cover the entire endwall using the same amount of coolant. The results indicated improvement in the majority of the passage endwall, but the coverage near the LE portion of the suction surface was still poor due to the horseshoe vortex and the suction side corner vortex. Later, the study of Barigozzi et al. [11] found that the passage vortex was weakened and cross flow in the passage was reduced with the increasing blowing ratio.

Upstream of the inlet guide vane, a gap (refer to **Figure 2**) commonly exists between the combustor and the vane endwall. Coolant air is often injected through these gaps, called inlet leakage, to prevent the ingestion of hot mainstream flow. This coolant air has a secondary effect of protecting the forward endwall region, and in some cases, the need for DFC holes can be reduced if this spent air can be used effectively. There have been a number of studies that investigated the effect of inlet leakage. An early study by Blair

[12] indicated that the film cooling effectiveness for the upstream slot injection varied greatly through the passage due to secondary flows. As a result, most of the coolant was swept across the passage toward the suction side corner resulting in a reduced cooling near the pressure side. However, the scope of the endwall cooling increases with the increasing coolant mass flow. Later, Granser and Schulenberg [13] found similar results and also concluded that the coolant from an upstream slot could lessen the strength of secondary flows in the passage as film reduced the boundary layer thickness. Burd and Simon [14] used the inclined slot for bleed injection, and their study showed that it encountered no aerodynamic penalty at all, rather, reduced the secondary flow effects. Later, Burd et al. [15] concluded from the similar study that a much higher coolant flow rate (6% of combustor bleed) could ensure better coverage over the most of the endwall. However, Oke et al. [16] found that a higher momentum flux is the key factor for forming that better coverage for the similarly inclined slot. Later, Oke and Simon [17] tried to control pitchwise coolant distribution by introducing the film from the multiple locations of a single or double row of slots to utilize the secondary flows. Their study indicated that at lower ratios of coolant-to-mainstream momentum flux, the film cooling flow migrates toward the suction side due to the secondary flow while higher ratios ensure a better coverage toward the pressure side endwall region. Again, Lynch and Thole [18] observed that a similar coolant coverage could be achieved by moving the slot further upstream of the vane. However, the effectiveness levels in the passage were lower for this configuration since the coolant has more distance to interact with the mainstream flow. Many studies of a double row of staggered cylindrical holes upstream of the LE have been

performed to simulate inlet leakage by Liu et al. [19], Oke et al. [20], Zhang and Jaiswal [21], and Zhang and Moon [22]. They all suggested that effectiveness was significantly improved with higher blowing ratio. Later, Zhang et al. [23] also investigated the effect of the cooling hole diameter and obtained an optimal value for their particular design.

To achieve an adequate coverage for the entire endwall, an upstream slot could be combined with the discrete holes. Knost and Thole [24] studied a vane passage endwall cooling for the inlet leakage flow including DFC holes and reported higher local effectiveness levels for the increased slot coolant flow.

Considering the real geometry, vanes are assembled as a unit of single or double airfoils to form an annular pattern depending on a specific design. An assembly interface is resulted, termed as a slashface gap. This gap is also pressurized by the coolant to minimize the ingestion of hot mainstream. Many studies have indicated a significant influence of slashface on the endwall cooling effectiveness. The aerodynamic loss attributed by a slashface gap was confirmed by Aunapu et al. [25]. They used blowing through a row of holes located at the passage centerline that reduced the influence of the passage vortex. Reid et al. [26, 27] also found a significant performance penalty by the slashface gap leakage relative to no gap leakage. However, they suggested that it can be improved if the gap is shifted toward the pressure side.

Ranson et al. [28] reported that the increasing coolant flow from a slashface gap provided minor cooling benefit to the overall platform. Later, Cardwell et al. [29] studied on the slashface gap sizes and reported that increasing the width of this gap reduced the coolant coverage on the endwall surface. Lynch and Thole's [30] endwall heat transfer results revealed that flow from this gap was mostly ejected near the throat resulting in a high heat transfer zone due to the formation of a small vortex. This vortex was also identified by Piggush and Simon [31, 32] which is responsible for the increasing passage losses.

Over the years, many efforts have been involved in providing sufficient protection on the vane endwall. Based on the above literature surveys, an endwall cooling design has been selected where discrete film cooling (DFC) hole patterns are engaged while making use of available in-built engine assembly interfaces. The objective of this work is to document the effect of coolant-to-mainstream mass flow ratio (MFR) and density ratio (DR) on endwall cooling where exit Mach number, inlet Reynolds number, and free-stream turbulence (FST) intensity closely simulated to real engine conditions. Additionally, the influence of a slashface gap within a passage is also studied in comparison to a passage without it. Although there have been many similar studies available including a wide range of different endwall cooling configurations, very limited or perhaps no studies have yet documented such details under engine-like flow conditions using PSP technique. Thus, this effort adds to the existing literature on the endwall cooling

of a gas turbine engine under realistic operating conditions and advances the understanding of the dynamic behavior of the endwall film cooling.

CHAPTER III

EXPERIMENTAL SETUP

This chapter provides a comprehensive description of the test facility and the experimental setup used for acquiring endwall film cooling data under the presence of engine-like flow condition. The experimental measurements were captured in a relatively small scale, high-speed wind-tunnel facility. Two different types of the investigation were conducted using the same test facility. Initially, the effect of leakage flows from slashface, and upstream gaps were studied with discrete film cooling holes. Later, four different endwall designs were used with only upstream leakage flow to study the full-coverage film cooling. The test condition allowed an inlet Reynolds numbers about 400,000 based on the axial chord and the approach velocity.

III.A TEST FACILITY DESCRIPTION

Objectives of this study require a test facility that produces close to engine-like flow conditions. **Figure 3** introduces the high-speed blow-down cascade facility located at the TEXAS A&M University. This facility operates under the room temperature and uses a high-pressure compressor (HPC) to supply mainstream air. This compressed air is routed to storage tank through a dryer system. Air is discharged from it in the blowdown mode at 250 psi and the target flow condition can reach inside the test section using a feedback controlled valve that ensures a steady flow for minimum 12 seconds (refer to **Figure 4**).

Supplied air then pushes through a circular duct followed by a diffuser. A flow conditioning duct is attached further downstream to achieve fully developed flow condition before passing through a square mesh turbulence grid. The grid has bar widths of 1.27 cm and spaced to form 3.22 x 3.22 cm^2 square openings with 48% porosity. It is installed at $2.72C_{ax}$ upstream of the vane LE plane producing an FST level of 19% with an integral length scale of about 1.7 cm at a downstream distance from the grid location of 14.5 bar width X/b = 14.5). As soon as the flow passes through the mesh grid, it enters the cascade and then exhausts through an exit duct.

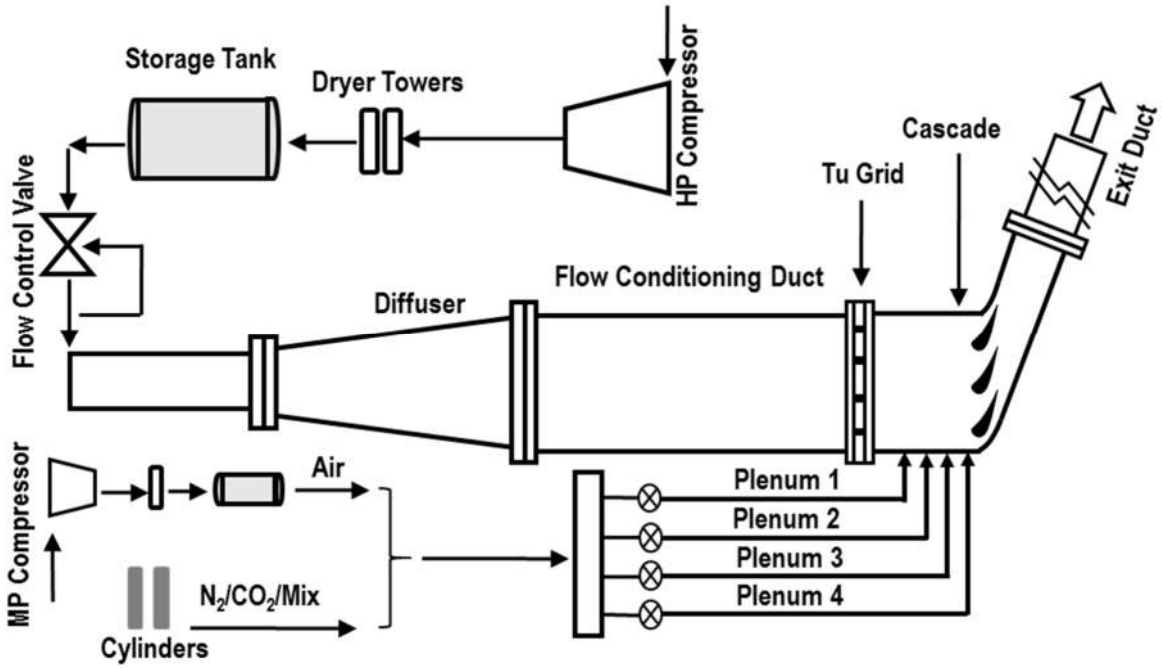

Figure 3 Schematic of experimental facility

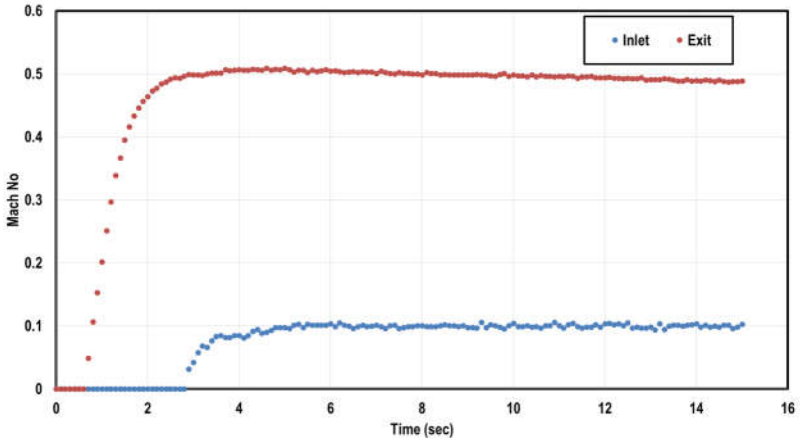

Figure 4 Flow conditions at the inlet and exit of the test section

The test section is a linear cascade consist of three vanes with two curved above the upper vane and below the lower vane that is resulting in four full passages. The entire test section is made of Aluminum. A row of 26 static pressure taps are spaced at 50% C_{ax} upstream of the LE plane, and another row of 25 taps are at 50% C_{ax} downstream from the TE plane to monitor the flow uniformity. The results confirmed an acceptable periodicity as shown in **Figure 5** and matched quite well with preliminary CFD predictions. The important cascade dimensions and mainstream flow conditions are listed in **Table 1**.

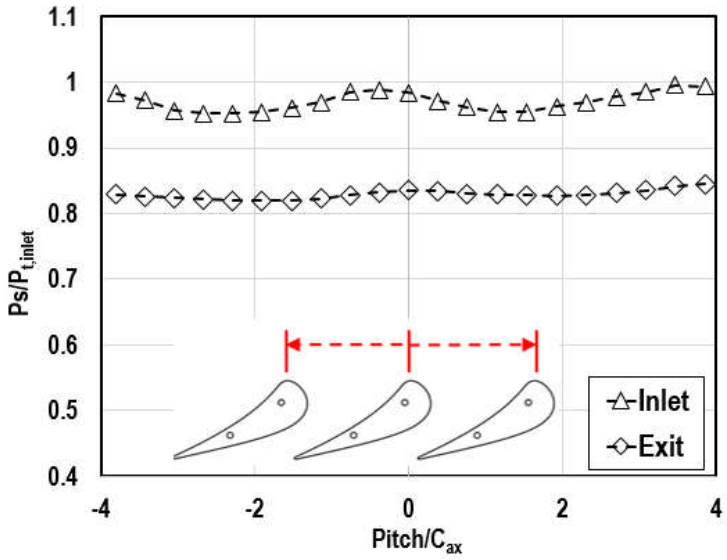

Figure 5 Pitchwise pressure distribution

Table 1 Geometric Parameters and Flow Conditions

Vane Geometry

Scale Factor	2	Solidity (C_{ax}/P)	0.63
True Chord, C (cm)	14.92	Aspect ratio (S/C)	0.82
Axial Chord, C_{ax} (cm)	8.28	Inlet Angle (deg)	0
Pressure Ratio (P_t/P_s)	1.192	Exit Angle(deg)	75.6

Mainstream Flow Conditions

Inlet Mach no., Ma_{in}	0.1	Inlet Reynolds no. Re_{in}	3.8×10^5
Exit Mach no., Ma_{ex}	0.5	Exit Reynolds no. Re_{ex}	1.7×10^6
FST Level, Tu (%)	19	Length scale, Λ_x (cm)	1.7

III.B INSTRUMENTATION

Inlet and exit velocities are monitored by two pitot-static probes stationed at 50% C_{ax} upstream of the LE and downstream of the TE. The mainstream mass flow rate is monitored based on the measured inlet velocity and corresponding cross-sectional area. Temperatures are monitored simultaneously using T-type thermocouples. Coolant supply plenums are equipped with separate rotameters to control coolant mass flow rate individually. Streamwise velocity fluctuations are measured to estimate the FST level and the corresponding length scale using a single hot-wire probe connected to a constant temperature anemometer. Hot-wire data are sampled at 80 kHz and filtered at 10 kHz. The endwall surface is painted with PSP (Innovative Scientific Solutions Inc., UF-750) by spraying 8-10 coats using an airbrush. To avoid reflection, the vanes are painted black and a transparent window is mounted on the top for the optical access. Two LED-based light sources with an optical wavelength of 400 nm (Innovative Scientific Solutions Inc., LM2X-DM-400) are used as the illumination sources. The lights are adjusted on the top of the test section to illuminate the target areas. Minimum interference is confirmed to achieve uniform intensity distribution over that entire surface. Upon excitation, the PSP coated surface emits light of wavelength around 650 nm. The emission intensity of coated surface is recorded through a long pass filter using scientific grade CCD camera (Innovative Scientific Solutions Inc., PSP-CCD-M, with 1608 x 1208 resolution, 35 fps, 14-bit dynamic range). A total of 100 gray scale images of emission intensity is considered to capture. In-house MATLAB codes can be used to average them and convert into pressure and then calculate film cooling effectiveness.

III.B.1. Temperature Measurement

T-type (copper-constantan) thermocouples were connected to a 16 channel 24- bit C series module (NI 9213) to measure the temperature in the tunnel and the plenums. Thermocouple readings were acquired through a compact data acquisition unit (cDAQ-9178) using a Labview program. The precision of the temperature reading is ±0.5ºC from the quoted specification.

III.B.2. Pressure Measurement

A Scanivalve pressure sensor module (as shown in **Figure 6)** with ± 0.15 percent FS quoted accuracy for ranges of 1.0 psi to 2.5 psi and ± 0.1 percent for 5 to 50 psi was used to measure pressures during the experiment. Total 32 ports can be scanned at a rate of 20 KHz and readings are monitored and recorded using a data acquisition unit.

Figure 6 ZOC 22b miniature pressure scanner (Courtesy: Scanivalve)

III.B.3. Hot Wire Measurements

Hot wire measurements were taken using a single wire at 50% C_{ax} upstream of the leading edge plane to record the mean and fluctuating velocities. Cable-equipped miniature 55P16 single wire probe with straight support and 1 m cable with BNC connector (refer to **Figure 7**) manufactured by Dantec Dynamics was used to obtain hot wire data. According to the manufacturer catalog (Finn E. Jørgensen 2002), the probe has a platinum-plated tungsten wire that is 5 μm in diameter and 1.25 mm in length. Hotwires must be calibrated before using for the test. The calibration technique is documented in Appendix A.

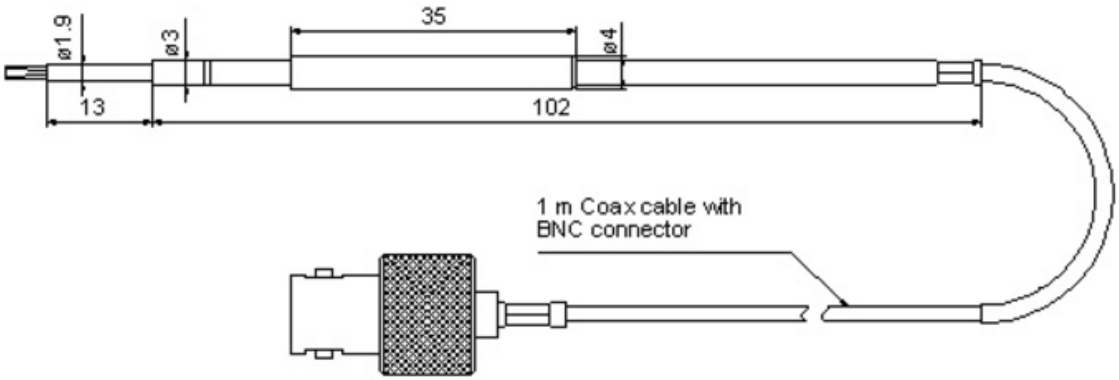

Figure 7 Cable-equipped miniature wire probe (55P16) (Courtesy: Dantec Dynamics)

A compact constant temperature anemometry (CTA) unit also from DANTEC DYNAMICS was used to operate the hot wire. Mean velocities and turbulence intensities were acquired and analyzed using a software package called StreamWare Basic. Velocity-

time data were recorded in 40 sets for each location whereas each set contained 8192 samples. Later, a Fast Fourier Transformation (FFT) was applied to map the time domain information to the frequency domain for spectral analysis.

III.B.4. PSP Measurement Technique

Principle

The static pressure distribution over a surface can be measured using PSP. PSP is comprised of photoluminescent molecules and an oxygen-permeable polymer binder, both dissolved in a solvent. When excited by a LED light source with a wavelength of 400 nm (violet color), then luminescent molecules in the paint emit photons at a wavelength around 650 nm as a relaxation from an excited state to their ground state. The emission intensity of painted surface is recorded using the optical technique. With the presence of oxygen molecules, luminescent molecules interact and transmit energy to oxygen molecules during their return to the ground state; this is known as oxygen quenching. In this radiation-less deactivation process, the intensity of the emitted light decreases with an increase in the concentration of oxygen (partial pressure) and this phenomenon serves as working principle for PSP. A typical PSP system is depicted in **Figure 8**.

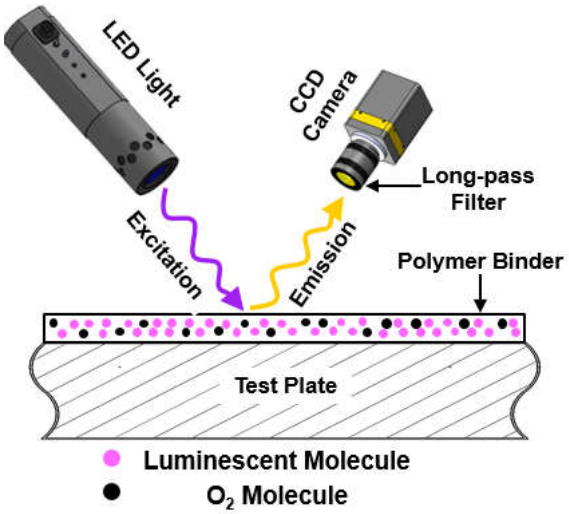

Figure 8 PSP working principle

Calibration

A CCD camera is used to record the emitted light intensity, then a relation between the partial pressure of oxygen (for the constant concentration of oxygen in the ambient air, this is equivalent to the partial pressure of air) and the emission intensity can be established by calibration. For calibration, a small strip of copper was first painted with black paint to reduce surface reflection and then painted with same layers of PSP coat as sprayed on the test piece. Later, that strip was placed inside a vacuum chamber with a transparent Plexiglas window on top for optical access. A T-type thermocouple was embedded in the strip and a flexible heater mat was attached to the other side of the strip. The distance and relative locations of LED lights and CCD camera to the copper strip were adjusted as close to as real experiment to ensure the similar view angle. However, PSP measurement is

insensitive to view angle effect reported by Shiau et al. [33]. This finding assures the accuracy of the PSP technique even though the perspective distortion may exist due to view angle disparity.

The CCD camera was set to capture 100 grey-scale images at each pressure to reduce the measurement noise. The emission intensity was then calibrated at several known pressures expected during the experiments ranging from -26 inHg (gauge pressure) to 8 psi (gauge pressure). Thus, the partial pressure of oxygen adjacent to the painted surface was correlated to the surface emission intensity by a curve fitting equation [Eq. 1].

$$\frac{I - I_{blk}}{I_{ref} - I_{blk}} = f\left(\frac{P_{O_2}}{P_{O_{2,ref}}}\right) = aX^b \qquad (1)$$

The emission intensity I correspond to a specific pressure, recorded during the calibration. The reference intensity, I_{ref} was the measured intensity under the reference pressure $P_{O_2,ref}$ (ambient pressure) with and I_{blk} is the intensity associated with the black images recorded under dark room condition considered as the background noise of the camera. However, the emitted light intensity is sensitive to both partial pressure of oxygen and temperature of the surface. To correctly report the uncertainty, the whole calibration processes were performed with test strip heated to different temperatures. According to the **Figure 9-a**, the emission intensity decreases as the surface temperature increases if the

reference condition is set at room temperature (unheated). It is found that if the reference condition is set at corresponding heated surface temperature, all the curves collapse into one as shown in **Figure 9-b**.

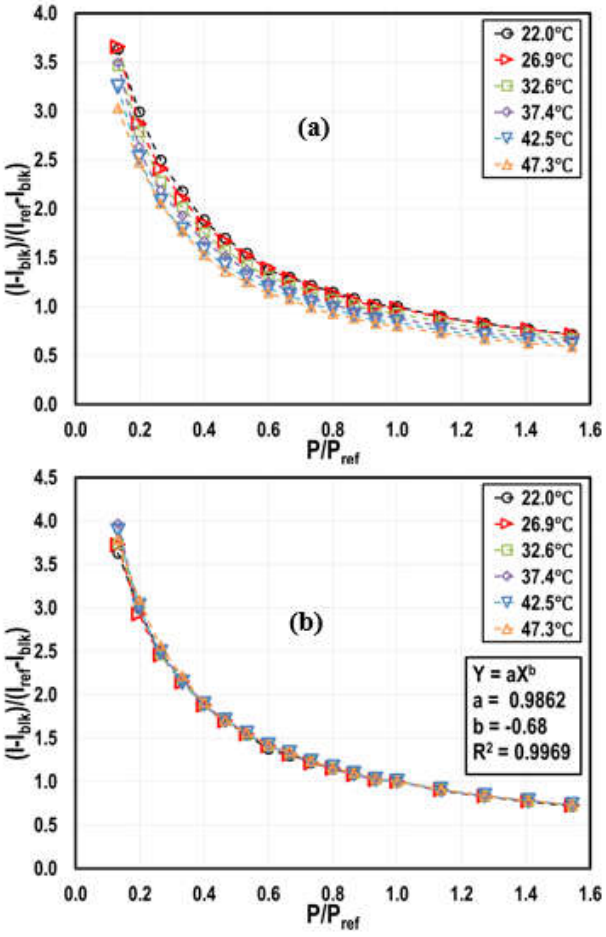

Figure 9 PSP Calibration results (a) T_{ref} = 22 °C; (b) T_{ref} is the same as operating temperature

The surface temperature in high-speed flow condition increases due to the aerodynamic heating, and it can be estimated as adiabatic wall temperature using

Equation 2. This elevated temperature may affect the PSP results due to the dependency of calibration curve on the surface temperature variation.

$$T_{aw} = T_s \left[1 + r\frac{\gamma - 1}{2} Ma^2\right] \quad (2)$$

For Ma_{ex} = 0.5, the maximum rise of the surface temperature in this study could be as high as 1.1°C. And it turns out that the corresponding effect is negligible.

III.C FUNDAMENTAL DATA ANALYSIS

III.C.1. Turbulence Measurements

A hot wire is capable of responding at very high frequencies which allow it to measure the turbulent fluctuations in the upcoming flow. The velocity in a turbulent flow field varies as a function of both space and time. Therefore, the use of statistical information is required to define any single point values of velocity. Details of the turbulence measurement parameters are described below [36].

Mean Velocity

The mean level of a signal which represents the average free stream velocity is denoted by, $\bar{u}$. Mathematically, it produces an average by summing a series of values

$$\overline{u} = \sum_{i=1}^{n} \frac{u_i}{n} = \lim_{T \to \infty} \frac{1}{T} \int_0^T u(t)dt \tag{3}$$

$$\overline{u^2} = \sum_{i=1}^{n} \frac{{u_i}^2}{n} = \lim_{T \to \infty} \frac{1}{T} \int_0^T u^2(t)dt = Mean\ Square \tag{4}$$

Velocity Fluctuation

To get the time average of the square of the fluctuation of the velocity about the mean yields the variance of the velocity, such as

$$\sigma^2 = \frac{\overline{(u - \overline{u})^2}}{n-1} = varience \tag{5}$$

$$\sqrt{\overline{u'^2}} = \left[\sum_{i=1}^{n} \frac{(\overline{u} - u_i)^2}{n-1} \right]^{1/2} \tag{6}$$

The independence of u_i is essential for statistical methods. From that standpoint, it is recommended to wait at least two or three integral time scales in between two samples to establish independence.

Autocorrelation

The autocorrelation in time is a measure of how well turbulence data is correlated among the points. The possibility of getting similar value at two points is high if they are

recorded very close in time. But any longer interval at least increases the probability of not having the two similar values. Autocorrelation coefficient is defined as

$$R_E\ (t) = \frac{\overline{u_1(t') * u_1(t'-t)}}{{u'_1}^2} \tag{7}$$

Equation 7 evaluated at every time interval (t) to generate an autocorrelation curve. The area under the curve given by **Equation 8** is the integral time scale of turbulence and defined as,

$$\tau_E = \int_0^\infty R_E\ (t)dt \tag{8}$$

Since the sample size is finite, **Equation 8** is evaluated only at first zero crossing of the autocorrelation curve. Typically, the integral length scale can be calculated from different approaches. But in this specific experiment, this scale is estimated based on Tylor's hypothesis, given in **Equation 9.**

$$\Lambda_x = \overline{u}.\tau_E \tag{9}$$

III.C.2. Film Cooling Effectiveness

To calculate film cooling effectiveness, two different coolants are required to inject independently. The air is used as one of the coolants while another can be any one of the oxygen-free foreign gases. As the foreign gas is injected, then it interacts with molecules on the PSP coated surface resulting in the variation of emitted intensity. The emitted intensity also measured from air injection case. From the difference in emitted intensity (i.e. partial pressure of oxygen) of injected air and foreign gas, film cooling effectiveness can be computed. Based on the heat and mass transfer analogy [34], film cooling effectiveness can be expressed as

$$\eta_{aw} = \frac{T_m - T_{aw}}{T_m - T_c} \approx \frac{C_m - C_w}{C_m - C_c} \approx \frac{C_{o_2,air} - C_{o_2,fg}}{C_{o_2,air} - C_{o_2,c}(\approx 0)} \tag{10}$$

$$\eta_{aw} = 1 - \frac{C_{o_2,fg}}{C_{o_2,air}} \tag{11}$$

The final form of the equation is obtained by replacing concentration terms with corresponding oxygen partial pressures:

$$\eta = 1 - \frac{1}{\left[\left(\frac{P_{O_2,air}/P_{O_2,ref}}{P_{O_2,fg}/P_{O_2,ref}} - 1\right)\frac{W_{fg}}{W_{air}} + 1\right]} \tag{12}$$

where $CO_{2,air}$ and $P_{O2,air}$ are the oxygen concentration and partial pressure with air injection, $CO_{2,fg}$ and $P_{O2,fg}$ are the oxygen concentration and partial pressure with foreign gas injection, W_{air} is the molecular weight of air, and W_{fg} is the molecular weight of the foreign gas.

Total four different sets (refer to **Table 3**) of the image are required to calculate the effectiveness. The capture time between the sets should be as less as possible to minimize any possible uncertainty.

Table 2 Different Image Conditions

Condition	LED	Mainstream	Coolant
1. Air (I_{air})	ON	ON	ON
2. Foreign gas (I_{fg})	ON	ON	ON
3. Ref. (I_{ref})	ON	OFF	OFF
4. Black (I_{blk})	OFF	OFF	OFF

CHAPTER IV

TURBINE VANE ENDWALL FILM COOLING WITH SLASHFACE LEAKAGE AND DISCRETE HOLE CONFIGURATION*

The chapter investigates the influence of leakage coolant from various gaps on the endwall film cooling performance under the variation of coolant-to-mainstream mass flow rate and density ratio. The vane endwall design includes inlet leakage gap (combustor-endwall interface) and slashface gap (interface between adjacent units) with DFC hole patterns. An assembly unit with two vanes is the focus of the present study and illustrated in **Figure 10**. The unit is arranged inside the cascade to form a slashface gap and this results with two complete passages (one complete and two halves) to reflect all the available features on it.

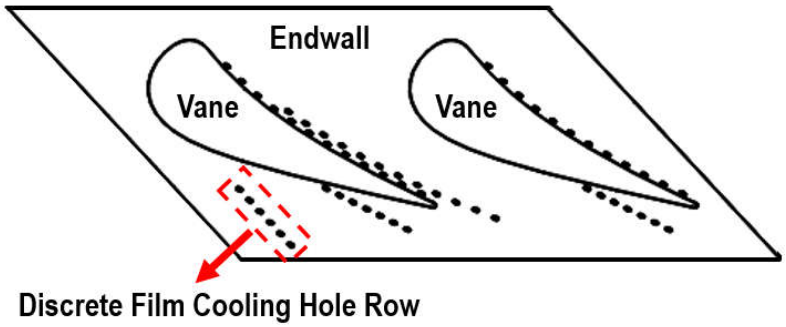

Figure 10 Vane assembly unit

---

* Reprinted with permission from Nafiz H. K. Chowdhury, C. C. Shiau and J. C. Han, L. Zhang and H. K. Moon, Turbine Vane Endwall Film Cooling with Slashface Gap and Upstream Inlet Leakage Flow Conditions, Journal of Turbomachinery 139(6):061003-061003-11 Copyright©2017 by ASME

IV.A TEST SECTION DESIGN

IV.A.1. Inlet Leakage Gap Simulator Design

Double rows of inclined (30°) and staggered holes are used to simulate inlet leakage feature as presented in **Figure 11**. The centerline of the second row is located at $0.7C_{ax}$ upstream of the vane LE plane. The film injection zone (width) covers two pitch distances with 68 holes. The holes are 0.254 cm in diameter (D), spaced by $3.5D$ in both the streamwise (X) and pitchwise direction (Y).

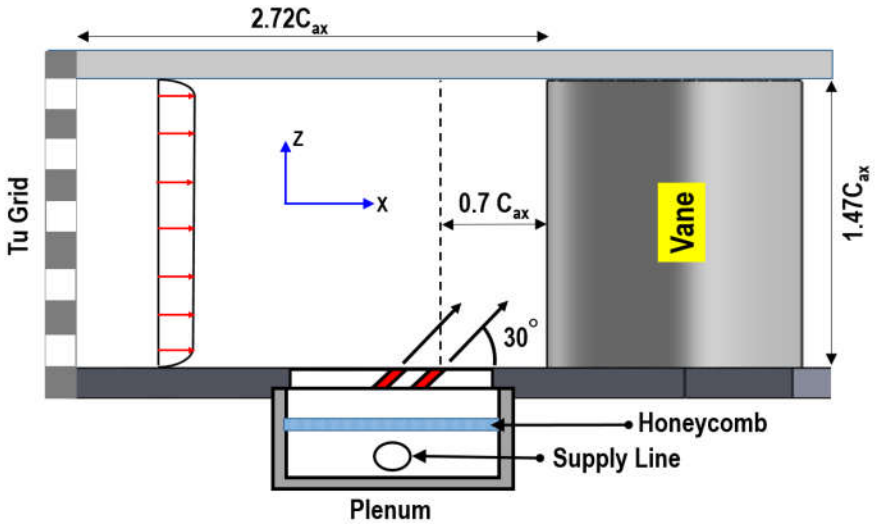

Figure 11 Schematic of inlet leakage simulation

IV.A.2. Slashface Design

The slashface gap is simulated by placing a slot on the endwall within a passage. The coolant is supplied to this gap from a plenum through a hole plate. This plate, containing a row of 20 discrete holes, is attached to the underneath of the cascade bottom endwall

and acts as the flow resistance characteristic of a typical seal, which is used in a gas turbine engine. The geometry of the gap and the hole plate are depicted in **Figure 12**.

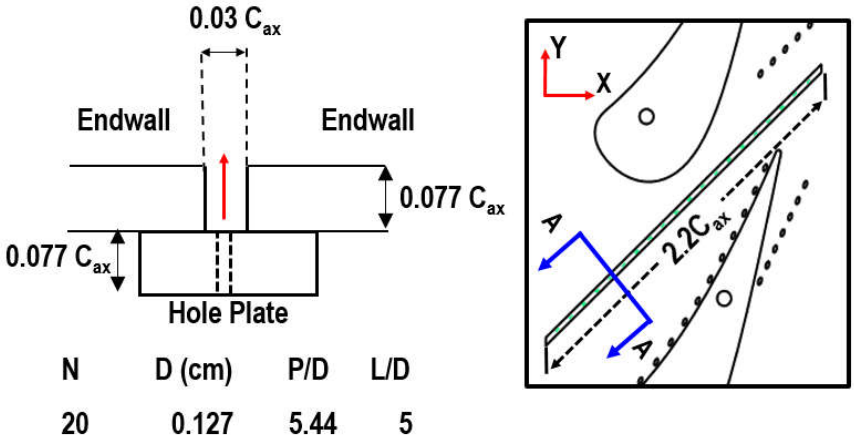

Figure 12 Slashface geometry

IV.A.3. Endwall Cooling Design

There are total six rows of discrete film cooling holes inside the two passages. The slashface passage has three rows R1, R2 and R3 while another passage without the slashface includes R4, R5 and R6. R1, R2 and R4 are placed near the downstream locations of the passages and intended to provide coverage toward the trailing edge (TE) wake region. Other rows (R3, R5 and R6) are located along the pressure side to obtain better coverage in the typical uncooled area of the endwall due to the cross flow effect. The cylindrical holes are at 30^{o} angle from the surface with an exit along the streamwise direction. The details are shown in **Figure 13**.

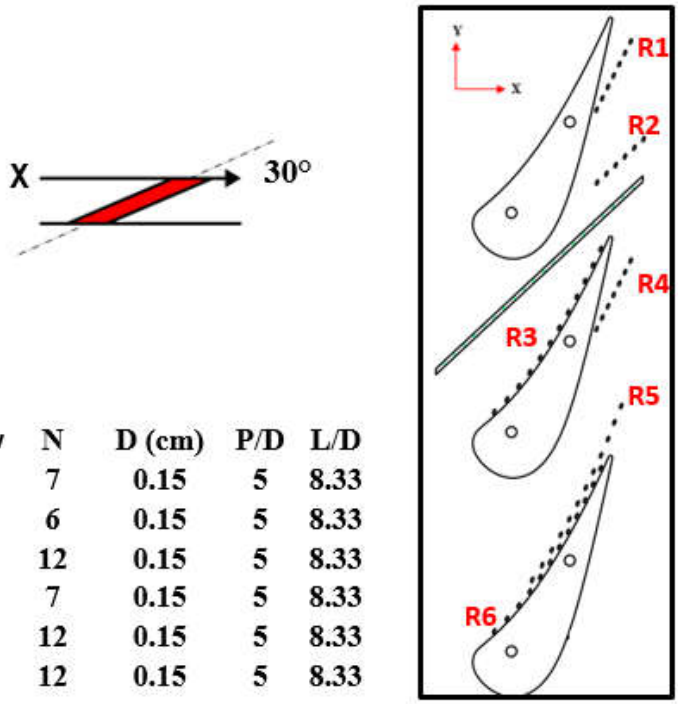

Row	N	D (cm)	P/D	L/D
R1	7	0.15	5	8.33
R2	6	0.15	5	8.33
R3	12	0.15	5	8.33
R4	7	0.15	5	8.33
R5	12	0.15	5	8.33
R6	12	0.15	5	8.33

Figure 13 Discrete film cooling hole pattern

IV.A.4. Plenum Designs

Four separate plenums are constructed underneath the bottom plate and can be controlled independently to introduce coolant to the corresponding locations. The plenum designs are illustrated in **Figure 14** where an individual one can be easily identified by the different floor color. One is for inlet leakage (blue), others are for passage with slashface (green), slashface leakage (red) and passage without slashface (yellow) accordingly.

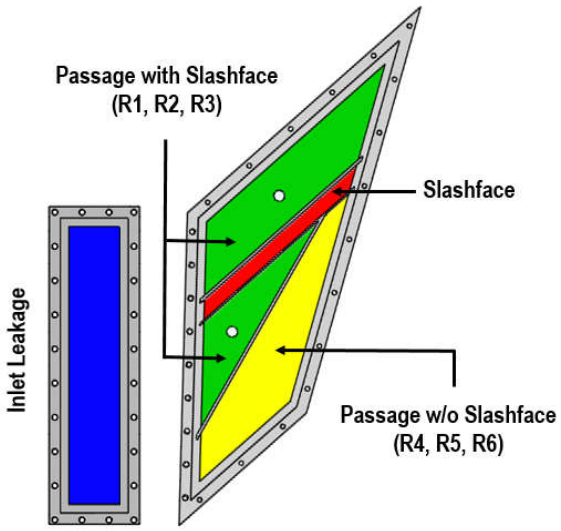

Figure 14 Top view of plenum designs

Honeycombs are installed inside them to distribute the coolant uniformly and multiple pressure taps are located to confirm it. Before the experiments, a leak test was conducted to ensure the proper sealing of the plenums. For supplying air as a coolant, multiple mid-range (125 psi) compressors are used. But for other coolants, industrial grade gas cylinders are used.

IV.B TEST CONDITIONS

A total of nine sets of the experiment for both phases is proposed to perform including a baseline (BL) case to study the effects of coolant to mainstream mass flow ratio (MFR (%)) and density ratio (DR) on the vane endwall cooling. The test conditions are summarized in **Table 3**. The variation of coolant density ratios is obtained using three different foreign gases (oxygen-free) including N_2, CO_2 and a mixture of *Ar* (85% by

volume) and SF_6 (15% by volume). The respective molecular weights are 1.0, 1.5 and 2.0 times of the corresponding mainstream air.

Table 3 Summary of Test Matrix

Case #	Leakage		Discrete Film-Cooling		DR
	Inlet	Slashface	w/ Slashface	w/o Slashface	
BL	**1.0%**	**0.5%**	**0.8%**	**1.0%**	**1.5**
1	0.5%	0.5%	0.8%	1.0%	1.5
2	1.5%	0.5%	0.8%	1.0%	1.5
3	1.0%	0.0%	0.8%	1.0%	1.5
4	1.0%	1.0%	0.8%	1.0%	1.5
5	1.0%	0.5%	0.4%	0.5%	1.5
6	1.0%	0.5%	1.2%	1.5%	1.5
7	1.0%	0.5%	0.8%	1.0%	1.0
8	1.0%	0.5%	0.8%	1.0%	2.0

IV.C RESULTS AND DISCUSSION

Primarily, the baseline is assessed by the detail film cooling effectiveness distribution on the endwall surface then MFR of inlet leakage, slashface leakage, and discrete film-cooling holes is then varied separately, and results are compared with that nominal case qualitatively and quantitatively. Second, density ratio effect is also evaluated in the same

manner. Finally, the quantitative comparison has been made to among all the variations to evaluate overall thermal performance.

IV.C.1. Pressure Measurement on Endwall Surface

Before measuring the film effectiveness data, the pressure distribution on the endwall is surveyed and presented in **Figure 15**. The pressure distribution is represented by the ratio of local static pressure and total inlet pressure. The local static pressure is measured by PSP while the total inlet pressure is measured by Pitot - static tube placed upstream of the LE plane.

The static pressure near the pressure side is higher than that of near the suction side in the contour plot. This differential pressure is the net driving force for the passage cross flow. The plot also shows a gradual decrease in pressure from the LE to the TE as the mainstream flow is accelerated. This non-uniform endwall pressure distribution affects the slashface gap leakage flow as well as the local coolant flow distribution from the discrete holes, especially, the rows close to the pressure side. And the higher pressure region close to the LE and along the pressure side of the passage has a tendency to prohibit the coolant injecting from this region if their corresponding momentum is not high enough.

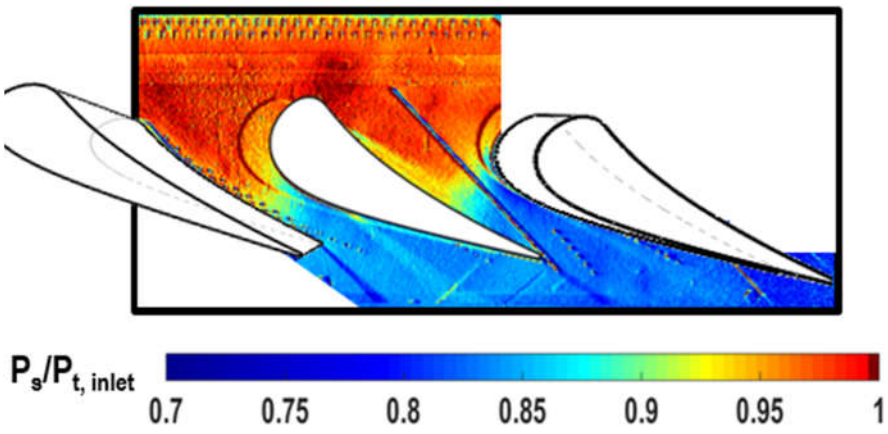

Figure 15 Static Pressure distribution by PSP

The local blowing ratio for inlet leakage, slashface gap and rows of discrete holes are defined as

$$M_{local} = \frac{(\rho V)_{c,local}}{(\rho V)_{m,local}} \tag{13}$$

Whereas $V_{c,\ local}$ is the actual coolant velocity obtained based on average discharge coefficient ($\bar{C}_d$). Initially, this coefficient was determined using **Equation 14** for total number of holes supported by a particular plenum where local pressures were used from **Figure 15**. This averaged value is assumed to be constant for all the corresponding holes.

$$\bar{C}_d = \frac{\dot{m}_{supplied}}{\sum_{j=1}^{N} P_o \left(\frac{P_{s,j}}{P_o}\right)^{\frac{\gamma+1}{2\gamma}} \sqrt{\frac{2\gamma}{(\gamma-1)RT_c}\left[\left(\frac{P_o}{P_{s,j}}\right)^{\frac{\gamma-1}{\gamma}} - 1\right]} \frac{\pi}{4} D^2} \quad (14)$$

Once the average value was determined then actual local coolant velocity from each hole is calculated to estimate corresponding blowing ratio. Later, an average blowing ratio for a specific row was computed. The values of $\bar{C}_d$ and M_{ave} is summarized in **Table 4**. Blowing ratio corresponding to the first hole ($M_{upstream}$) and as for last hole ($M_{downstreame}$) for a specific row or slashface are included for information.

Table 4 Coolant Flow Parameters

Location	**MFR**	$\bar{C}_d$	$M_{upstream}$	$M_{downstream}$	M_{ave}
Inlet Leakage	1.0%	0.71	-	-	0.76
Slashface	0.5%	0.8	0.70	0.83	0.77
R1	0.8%	0.65	0.62	0.62	0.62
R2		0.65	0.62	0.62	0.62
R3		0.65	0.60	0.62	0.59
R4	1.0%	0.58	0.58	0.59	0.59
R5		0.58	0.60	0.58	0.59
R6		0.58	0.61	0.59	0.6

IV.C.2. Effect of Inlet Leakage MFR

Film cooling effectiveness distribution due to all the three MFR cases for upstream inlet leakage is presented in **Figure 16** while MFR for slashface gap and discrete holes (DFC) are at baseline condition. As the inlet leakage location is far (X/C_{ax} = - 0.7) from the upstream so the coolant distribution across the pitch is uniform and has minor tendency to be affected by the horseshoe vortex. The effectiveness distribution serves as a means of flow visualization that can help to understand the interaction between the cooling jets and secondary flow. As the film approaches the passage, shifting tendency from the pressure side of the vane to the suction side is observed for all the cases. As MFR goes up, the jet moves with higher momentum that reduces the strength of horseshoe vortex and can penetrate further

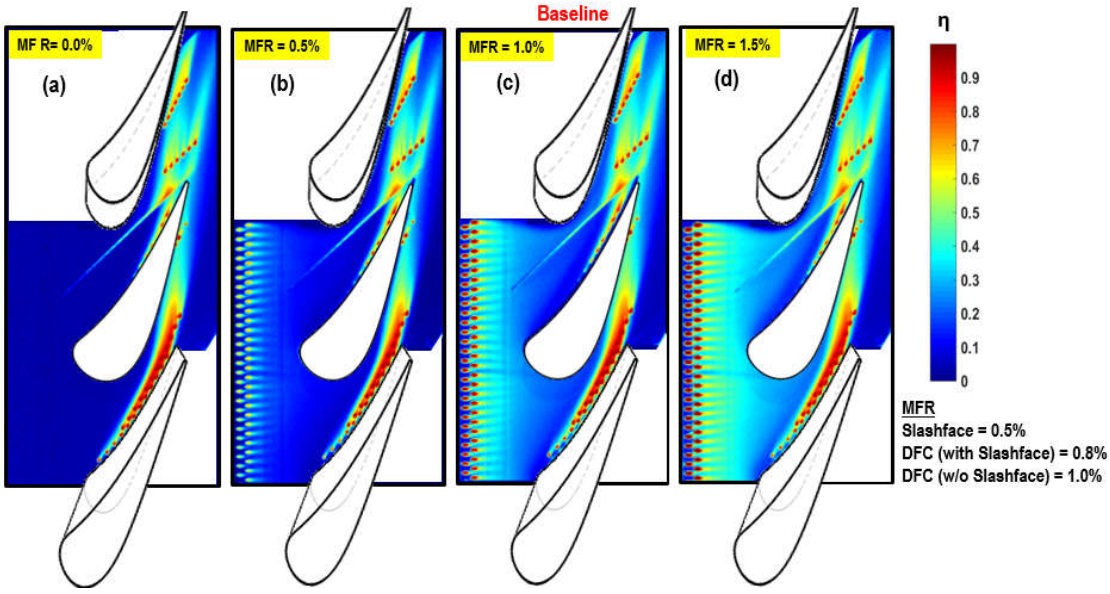

Figure 16 Endwall film effectiveness contours for inlet leakage MFR of (a) 0.0%; (b) 0.5%; (c) 1.0 %; (d) 1.5%.

downstream inside the passage resulting an extended coverage toward the pressure side similar to the results of Blair [12] and Burd et al. [14]. The downstream passage and TE portion are benefited by the film coverage from slashface and discrete film cooling holes for all three cases. For 1.5% MFR leakage jet merges with them and produce continuous uniform coverage. **Figure 17** shows the corresponding pitchwise averaged film cooling effectiveness distribution. Higher inlet leakage flow results in significant increase in averaged film cooling effectiveness levels compare to lower one. However, the effectiveness decays right downstream of the injection hole location. The level of effectiveness keeps decreasing when it approaches inside the passages. The effectiveness increasing trend in two passages is different. For the passage with slashface, the contribution initiated from X/C_{ax} = 0.2 and continues till X/C_{ax} = 0.8. Then overall effectiveness for all the flowrates drops from slashface, and discrete film cooling hole injection benefits the effectiveness from X/C_{ax} = 0.5. On the other hand, for the passage without slashface, the effectiveness enhancement by discrete film cooling hole gradually.

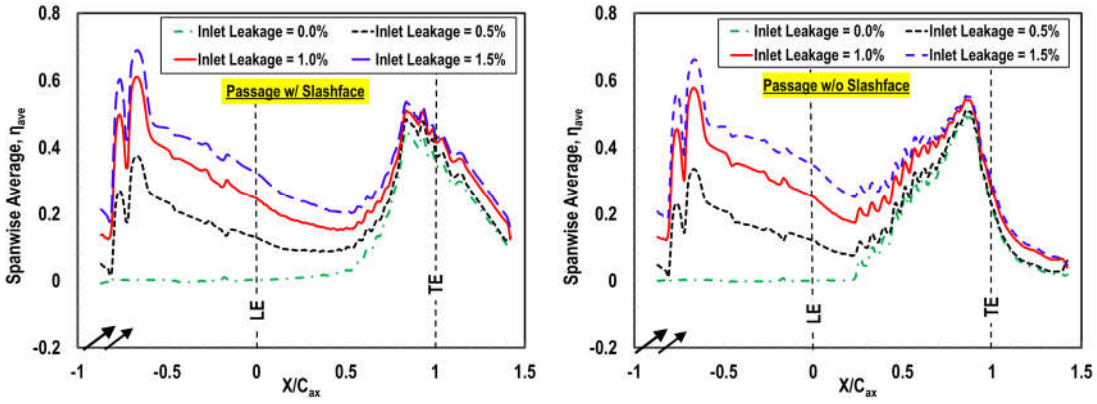

Figure 17 Pitchwise average endwall film cooling effectiveness for varying IL MFR

IV.C.3. Effect of Slashface Leakage MFR

Film cooling effectiveness distributions for slashface leakage at different mass flow ratios are presented in **Figure 18** while the flowrates for inlet leakage and discrete holes are as same as the baseline case. For this study, only passage that includes slashface is expected to be affected. For no slashface leakage (**Figure 18-a**), a significant reduction is observed near the downstream of the throat region compare to the baseline case. **Figure 18-a** also indicates a low effective zone between R1 and R2; R2 and R3. Also, without the ejection the slashface feature acts as a gap to locally trip the flow, which leads to the discontinuity in R3 coolant trace shown in **Figure 18-a**. As the MFR increases, the coverage goes up and shows substantial improvement in the downstream of slashface near the throat region. Nevertheless, the effect of higher MFR diminishes as soon as the flow passes TE plane. At MFR = 1.0%, the slashface injects coolant in a non-uniform manner along its length in **Figure 18-c**.

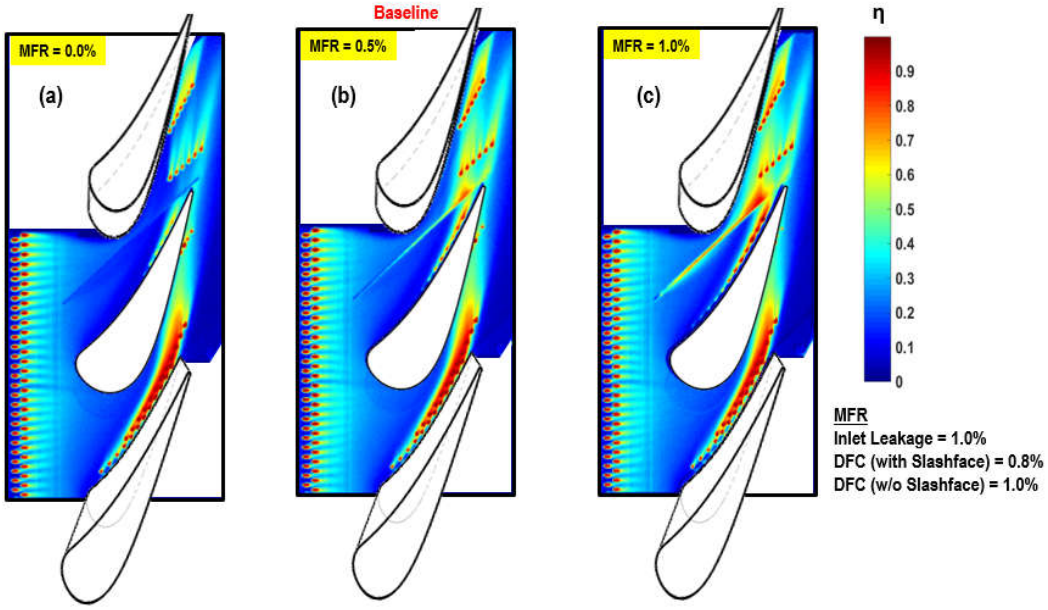

Figure 18 Endwall film effectiveness contours for slashface MFR of (a) 0.0%; (b) 0.5%; (c) 1.0 %

Piggush and Simon [31] observed the ingestion of the mainstream into the slashface until X/C_{ax} = 0.42 inside the contoured passage for MFR= 0.5% and then coolant injects. However, in this study, the corresponding plenum pressure is quite higher than the upstream part (outer endwall) of the slashface where the highest static pressure is observed (**Figure 15**). Therefore, the ingestion is unlikely the situation happened in this study as illustrated in **Figure 18-b**. The inlet leakage MFR = 0% (**Figure 18-a**) discussed in the previous section also demonstrates that the coolant ejections happen from the very beginning (upstream) of the slashface. As MFR goes up to 1.0%, the injected coolant tends to leave the gap directs toward the vane pressure side, and then travel toward the suction side of the adjacent airfoil similar to the results observed by Ranson and Thole [28]. It is most likely the cross flow effect caused by the interaction of streamwise velocity vector

with coolant jet that comes out of slashface gap with higher momentum. This interaction results in higher mixing which may spill off some coolant toward the pressure side locally. Then the passage cross flow sweeps the coolant toward the suction side.

The endwall static pressure distribution dominates the gap leakage flow trajectory, as the lower static pressure near the throat region can be seen (**Figure 15**), most of the flow tends to leave from this region. Such phenomena is consistently shown for gap MFR = 0.5% and 1.0%. A substantial amount of coolant is coming out of the downstream part of slashface gap with a wedge shape structure toward the Suction side. As the flowrate increases the shape also swells but distorts toward the TE plane due to the mainstream flow direction. This wedge shape region provides better coverage with very high effectiveness, but in the meanwhile, it is expected to augment the heat transfer and possibly the losses due to the excessive flow mixing. On the other hand, the behavior of discrete holes near the pressure side (R3) also shows certain dependency to the variation of MFR. With the increment in MFR, more holes upstream of the row can inject coolant as traces are obvious from the **Figure 18**. It is probably due to the change in the near-wall flow field structure as slashface leakage interact with mainstream flow.

The plots for pitchwise averaged cooling effectiveness have been shown in **Figure 19**. It demonstrates that slashface gap leakage has a significant effect on film effectiveness as it improves with increasing MFR, especially for the corresponding passage. It also

indicates that the passage without slashface is not affected by the range of slashface gap flowrates as the boundary conditions are the same for it.

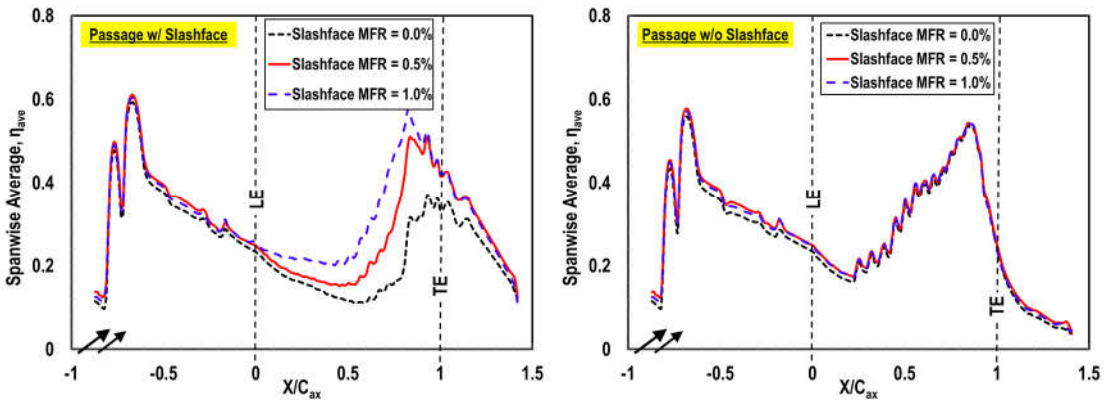

Figure 19 Pitchwise average endwall film cooling effectiveness for varying slashface MFR

IV.C.4. Effect of Discrete Hole Coolant MFR

Film cooling effectiveness distribution for discrete film-cooling hole patterns in both passages have been illustrated in **Figure 20** at different flowrates with MFRs for leakage flow from slashface, and inlet leakage gaps are kept at baseline condition. For the lower value of MFR, **Figure 20-a** shows a significant reduction in effectiveness from poor coverage. Especially, near the pressure side for both passages, an uncooled region can be seen due to the strong cross flow. This uncooled region diminishes as MFR increases. With the increase in MFR, the corresponding momentum also increases that helps coolant to overcome the relatively higher static pressure regions. As a result, coolant can come out of the upstream holes for R3, and R6.

Figure 21 shows the corresponding pitchwise averaged cooling effectiveness in the streamwise direction. Passage without slashface is a bit different as the MFR is relatively higher than the passage with slashface and more holes are observed to discharge coolant systematically. For passage with slashface the response to MFR change is quite significant compared to the adjacent passage, especially at higher MFR. It is noteworthy to see the zigzag region within the passage in **Figure 21** which indicates the local effectiveness peaks just downstream of the hole injection locations. For higher flowrates, the aforementioned wedge above shape also increases as significant coolant gathers by the contribution of neighbor holes injection.

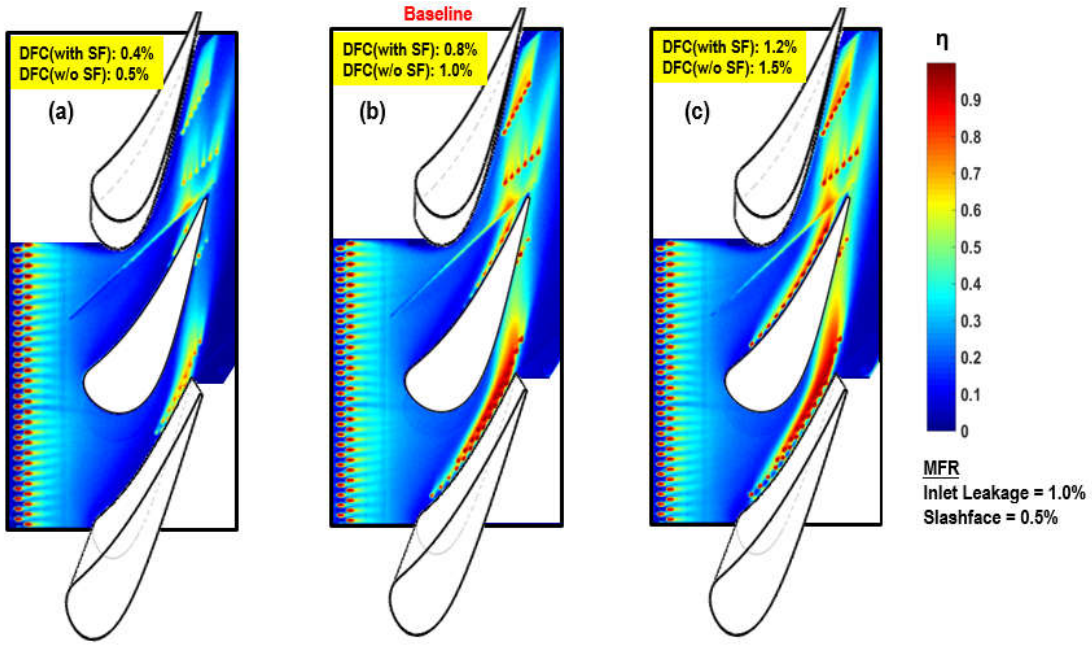

Figure 20 Endwall film effectiveness contours for discrete hole injection MFR of (a) DFC (with slashface) = 0.4%, DFC (w/o slashface) = 0.5%; (b) DFC (with slashface) = 0.8%, DFC (w/o slashface) = 1.0%; (c) DFC (with slashface) = 1.2%, DFC (w/o slashface) = 1.5%

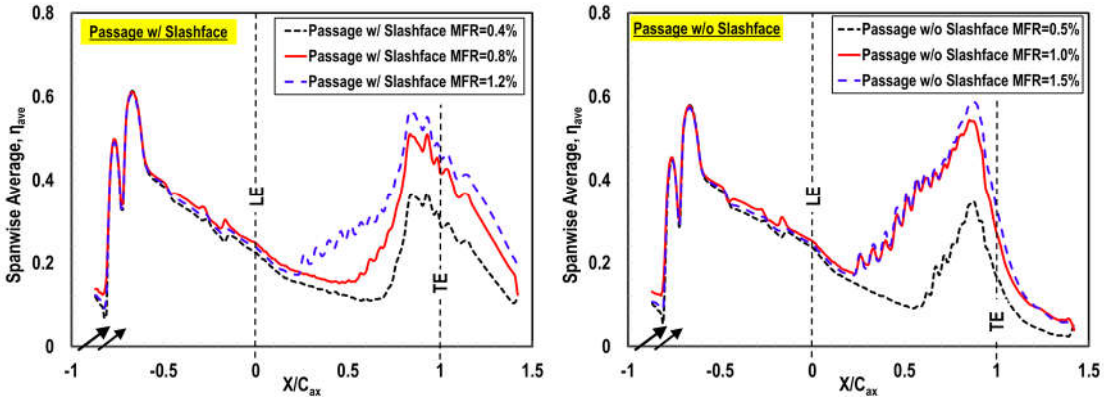

Figure 21 Pitchwise average endwall film cooling effectiveness for varying discrete hole MFR

IV.C.5. Effect of Density Ratio

Figure 22 presents the film cooling effectiveness contours for increasing density ratios. The baseline values are maintained for all the flowrates. As the inlet leakage injection located in a relatively uniform cross section of the inlet with a blowing ratio of 0.73, DR effect on this region is expected to behave as cooling holes on the flat plate. **Figure 22** also indicates the lateral spreading of leakage jet is enhanced as DR increases. Better coolant coverage provides fairly uniform effectiveness distribution in the pitchwise direction.

But slashface gap leakage and coolant from discrete holes in both passages demonstrate different characteristics due to lower local blowing ratios. For the same blowing ratio, an increase in density ratio reduces the momentum of the coolant for the

same blowing ratio; therefore, the coolant bears insufficient momentum and thus, fail to deliver through the holes located in the relatively high-pressure region. It is possibly the situation seen in upstream of R4 and R6 rows shown in **Figure 22-c**.

The line plots of average film effectiveness for all three DRs have been presented in **Figure 23**. It shows that initially the effectiveness value is higher for higher density ratios, however, 1.5 and 2.0 are quite comparable to each other and continue the trend until X/C_{ax} = 0.5. But right after this point, DR = 2.0 shows reduced performance compare to 1.0 and 1.5. **Figure 22-c** shows a reduction in the number of upstream injecting holes for R3 and R6. As a result, the average effectiveness is also affected. However, since the coolant injection amount is the same for all density ratios, the identical peak levels near X/C_{ax} = 0.85 are observed due to the coolant accumulation.

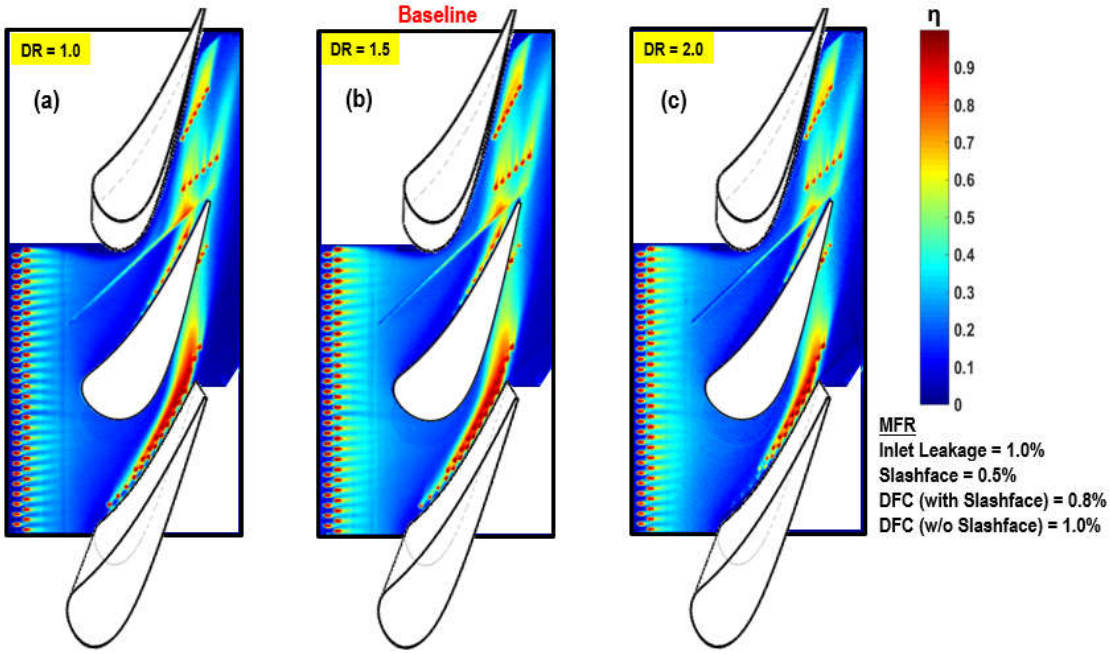

Figure 22 Endwall film effectiveness contours for density ration of (a) 1.0; (b) 1.5; (c) 2.0

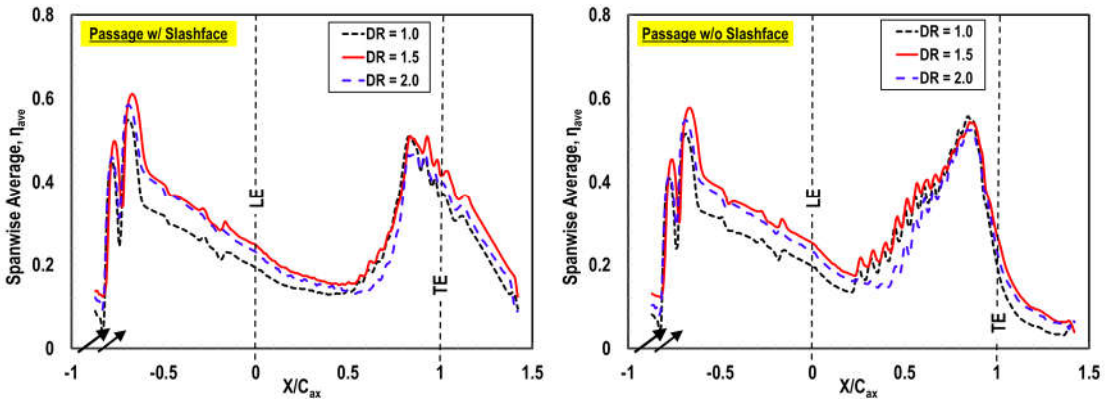

Figure 23 Pitchwise average endwall film cooling effectiveness for varying density ratio

CHAPTER V

ENDWALL FILM COOLING STUDY FROM VARIOUS DISCRETE HOLE CONFIGURATIONS WITH SIMULATED UPSTREAM LEAKAGE FLOW*

The primary objective of this chapter is to investigate the film cooling performance of different full-coverage film cooling designs with inlet leakage flow. A reduced number of holes per passage has been selected for all the designs. Four different configurations including axial row (AR) and cross row (CR) with two different cluster patterns are the focus of this study.

V.A TEST SECTION DESIGN

V.A.1. Inlet Leakage (IL) Gap Simulator Geometry

Double rows of inclined (30^o) and staggered holes are used to simulate upstream combustor-endwall gap as presented in **Figure 24**. The hole diameter is 0.175 cm with a hole-to-hole spacing of 4D in both the streamwise (X) and pitchwise direction (Y). This configuration provides a higher velocity ratio (=1) at DR = 1.5. The film injection zone covers two full passages with 75 holes and the centerline of the second row is located at $0.38C_{ax}$ upstream of the vane LE plane.

---

* Reprinted with permission from Nafiz H. K. Chowdhury, C. C. Shiau and J. C. Han, L. Zhang and H. K. Moon, Turbine Vane Endwall Film Cooling From Axial-Row Configurations with Inlet Leakage Flow, ASME Turbo Expo 2017, Charlotte, NC, USA, GT2017-63144, Copyright©2017 by ASME

*Reprinted with permission from Nafiz H. K. Chowdhury, C. C. Shiau and J. C. Han, L. Zhang and H. K. Moon, Turbine Vane Endwall Film Cooling From Cross-Row Configurations with Inlet Leakage Flow, ASME Turbo Expo 2017, Charlotte, NC, USA, GT2017-63145, Copyright©2017 by ASME

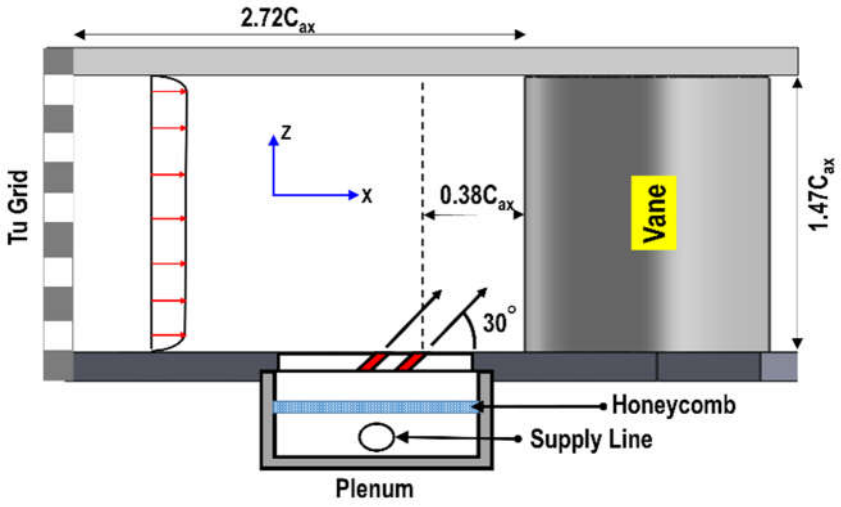

Figure 24 Schematic of upstream inlet leakage simulator

V.A.2. Endwall Cooling Design

Total four different endwall (EW) cooling patterns – i) axial row and cross row; ii) cluster A and cluster B were selected for this study. All these patterns were produced on a removable test piece, made from an ultra-tough resin material called Accura® Xtreme™ White 200 using stereolithography (SLA) process. A fine resolution was selected for manufacturing the part with a smooth surface finish.

Axial Row (AR) and Cross Row (CR) Arrangements

Schematic of AR and CR configurations is illustrated in **Figure 25**. There are three rows (Row 1, Row 2 and Row 3) of total 18 cylindrical holes oriented in the axial direction called axial-row (AR) configuration. The surface angle (α) for all the cylindrical holes is

30° with an exit angle of 20° from the pitch line (*Y* axis). For the CR configuration, total 18 cylindrical holes are oriented in cross flow direction called cross row (CR) configuration. The details are provided in **Table 5**.

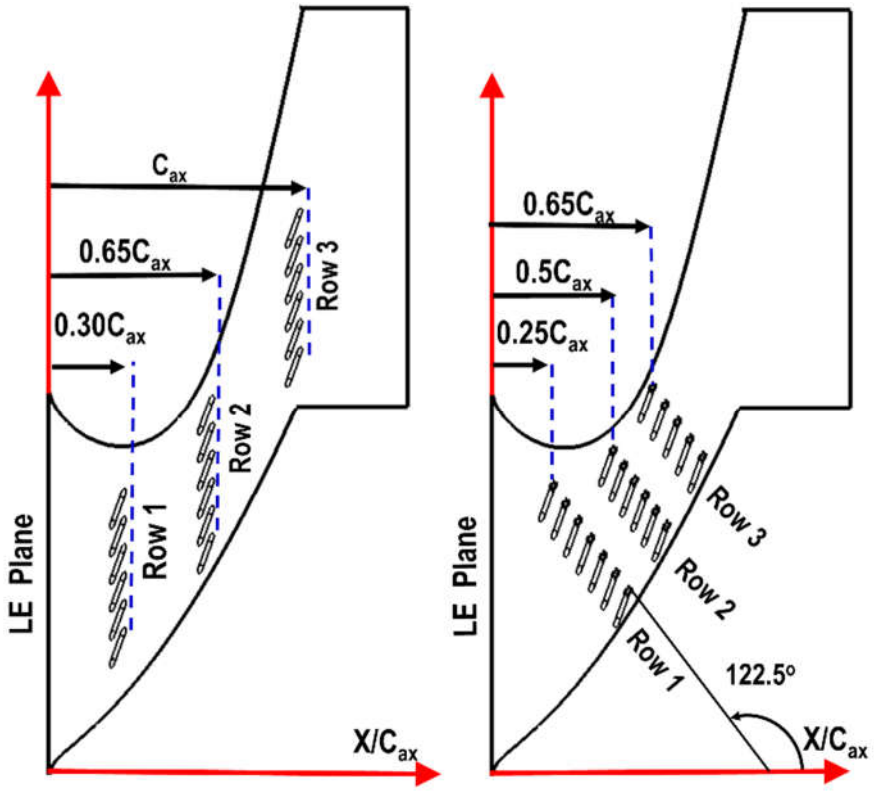

Figure 25 Schematic of passage cooling designs a) AR configuration and b) CR configuration

Table 5 Hole Geometry

Parameter	Row1/Row2/Row3
Diameter, *D* (cm)	0.15
Pitch to dia. ratio, *P/D*	6/6/6 (AR), 4.5/4.5/4.5 (CR)
Surface angle, α (deg)	30
Hole exit angle, β (deg)	20
Length to dia. ratio, *L/D*	8.33
Total holes, *N*	6/6/6 (AR), 7/6/5 (CR)

Cluster A and B configurations

Schematic of cluster configurations is illustrated in **Figure 26**. There are total 18 holes arranged in four groups (G1, G2, G3 and G4) for cluster A and six groups (G1, G2, G3, G4, G5 and G6) for cluster B. Surface angle and exit angle are as same as the AR and CR configurations. Holes located next to the PS curve are two hole diameter away from the PS curve. The details are provided fin **Table 6**.

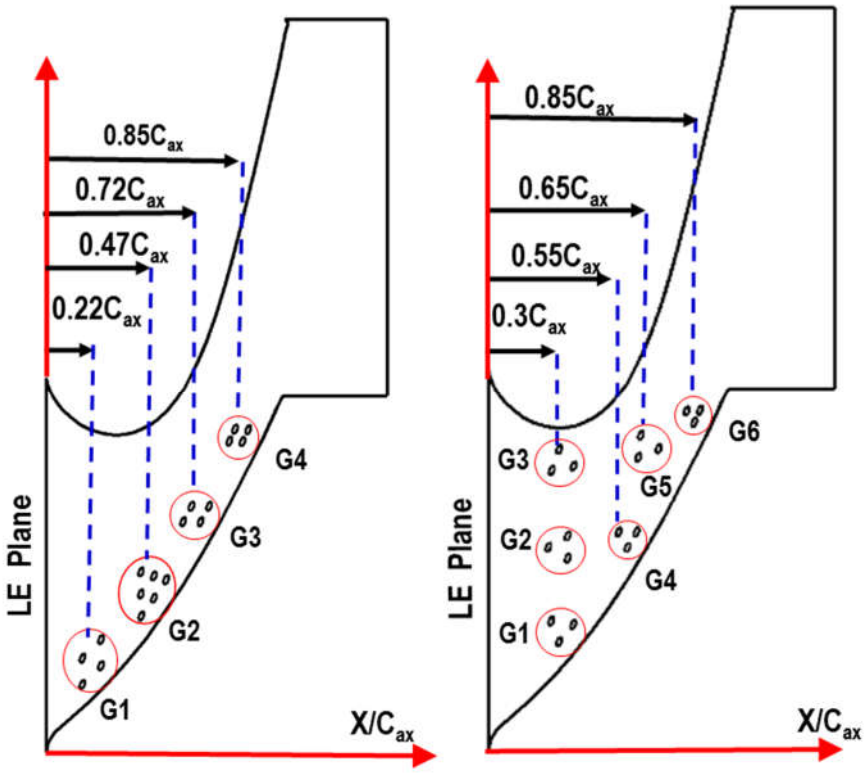

Figure 26 Schematic of passage cooling designs a) Cluster A; b) Cluster B

Table 6 Hole Geometry Details

Parameter	Cluster A-G1/ G2/G3/G4, Cluster B-G1/ G2/G3/G4/G5/G6
Diameter, *D* (cm)	0.15
Pitch to dia. ratio, *P/D*	6/5/4/3, 5/5/5/4/5/3
Surface angle, α (deg)	30
Hole exit angle, β (deg)	20
Length to dia. ratio, *L/D*	8.33
Total holes, *N*	4/6/4/4, 3/3/3/3/3/3

V.A.3. Plenum Designs

Plenums are designed using aluminum. Special considerations are applied during the design process due to the space limitations and leaking tendency as high-pressure coolant is supplied. Initially, air enters inside the plenums and passes through the wire mesh screen and honeycomb respectively to straightening the flow and achieve uniformity. Plenums for inlet leakage and endwall are represented in **Figure 27**.

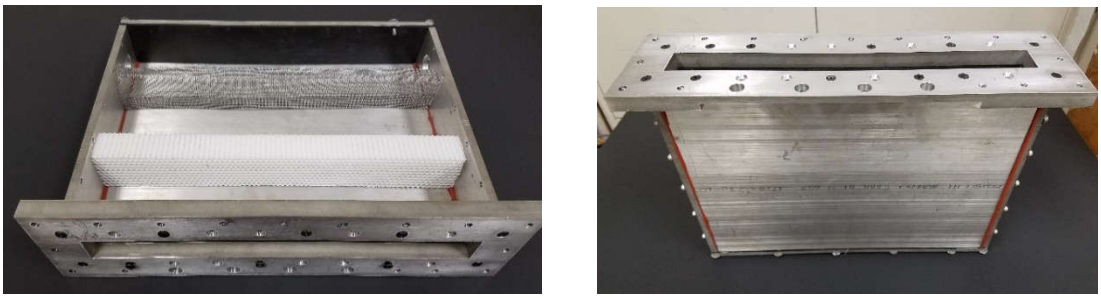

Inlet leakage plenum

Endwall leakage plenum

Plenum Assembly

Figure 27 Plenum designs

V.B TEST CONDITIONS

A total set of nine experiments were performed including a baseline (BL) case to study the effect of coolant-to- mainstream mass flow ratio (MFR (%)) and density ratio (DR) on the vane endwall cooling. Initially, the BL case was evaluated under DR = 1.5 and then additional eight cases were made-up to compare with the BL case. The test conditions are summarized in **Table 7**. The variation of coolant density ratios was obtained using three different foreign gases (oxygen-free) including N_2, CO_2 and a mixture of Ar (85% by volume) and SF_6 (15% by volume). The respective molecular weights are 0.97(≈ 1.0), 1.52(≈ 1.5) and 1.93(≈ 2.0) times of the corresponding mainstream air.

Table 7 Summary of Test Matrix

Case #	MFR (%)			DR
	Leakage (IL)	Passage (EW)	∑	
BL	***1.0***	***1.0***	***= 2.0***	***1.5***
1	-	1.0	=1.0	1.5
2	0.5	1.0	= 1.5	1.5
3	1.5	1.0	= 2.5	1.5
4	1.5	-	= 1.5	1.5
5	1.0	0.5	= 1.5	1.5
6	1.0	1.5	= 2.5	1.5
7	1.0	1.0	= 2.0	1.0
8	1.0	1.0	= 2.0	2.0

V.C RESULTS AND DISCUSSION

Primarily, detailed film cooling effectiveness distributions on the endwall surface are discussed for a range of cooling flow rates from the inlet leakage and endwall design separately. Density ratio effect is also discussed in the similar fashion. Finally, the area-averaged values are presented for all the cases.

V.C.1. Axial Row (AR) Configuration

Prior to the experiments, the static pressure distribution on the endwall was obtained using the commercially available computational fluid dynamics (CFD) package STAR-CCM+ 13.0. The pressure distribution is presented in **Figure 28** by the ratio of local static pressure and total inlet pressure. The static pressure near the pressure side is higher than that of near the suction side in the contour plot. This differential pressure is the net driving force for the passage cross flow. The plot also shows a gradual decrease in pressure from the LE to the TE as the mainstream flow is accelerated.

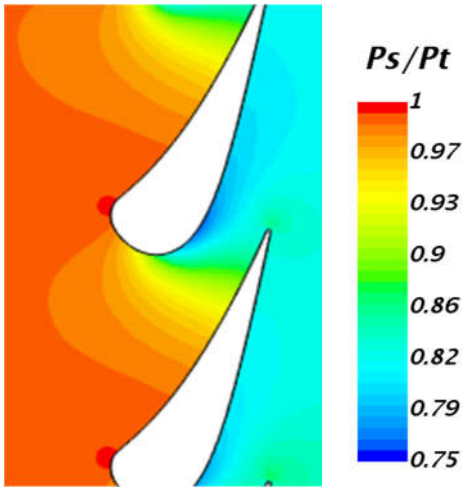

Figure 28 Static pressure distribution from CFD

The result of the baseline case is shown in **Figure 29** with calculated inviscid streamlines and lift-off line of the pressure side horseshoe vortex which is detected at IL MFR = 0.5% (black dashed line). Lift-off line is expected to shift slightly as the tracer gas is injected at MFR of 0.5%. An original image from the camera with hole exit directions is also provided in the figure for the perspective view of the target area.

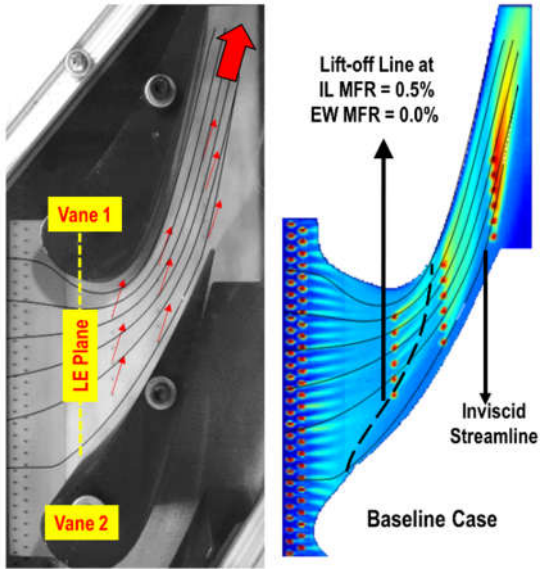

Figure 29 Original camera view with flow visualization

Local Blowing Ratio Distribution

A non-uniform pressure distribution is pronounced to have a significant influence on the local injection trajectory when multiple holes within a passage are supported by a single plenum. Then, parameters like blowing and momentum flux ratios experience large variations in both the streamwise and pitchwise directions. A clear understanding of those

parameters is required before discussing the results. In this particular study, local values were calculated using **Equations 15** and **16**.

$$M_{local} = \frac{(\rho_c V_c)_{local}}{(\rho_m V_m)_{local}} \tag{15}$$

$$I = \frac{\rho_c {V_c}^2}{\rho_m {V_m}^2} = \frac{M^2}{DR} \tag{16}$$

Whereas $V_{c,\,local}$ is the actual coolant velocity obtained based on the average discharge coefficient ($\bar{C}_d$). Initially, this coefficient was determined using **Equation 14** for total number of holes supported by a particular plenum where local pressures were ($P_{s,j}$) used from **Figure 28** and the plenum total pressure directly measured from the experiments. Then, this averaged value is assumed to be constant for all those corresponding holes.

Once the average value was determined then actual local coolant velocity from each hole is calculated to estimate the corresponding local value of blowing ratio. The local values are reported in **Figure 30** for all EW MFRs. As the leakage cooling hole rows are located within a very low-velocity zone, then average blowing ratios are considered. The corresponding average blowing ratios are 0.72, 1.48 and 2.22 at *MFR* = 0.5%, 1.0% and 1.5% accordingly.

Due to the lower static pressure on the suction side region as well as the downstream part of the passage (as flow accelerates) higher coolant mass flux should be observed

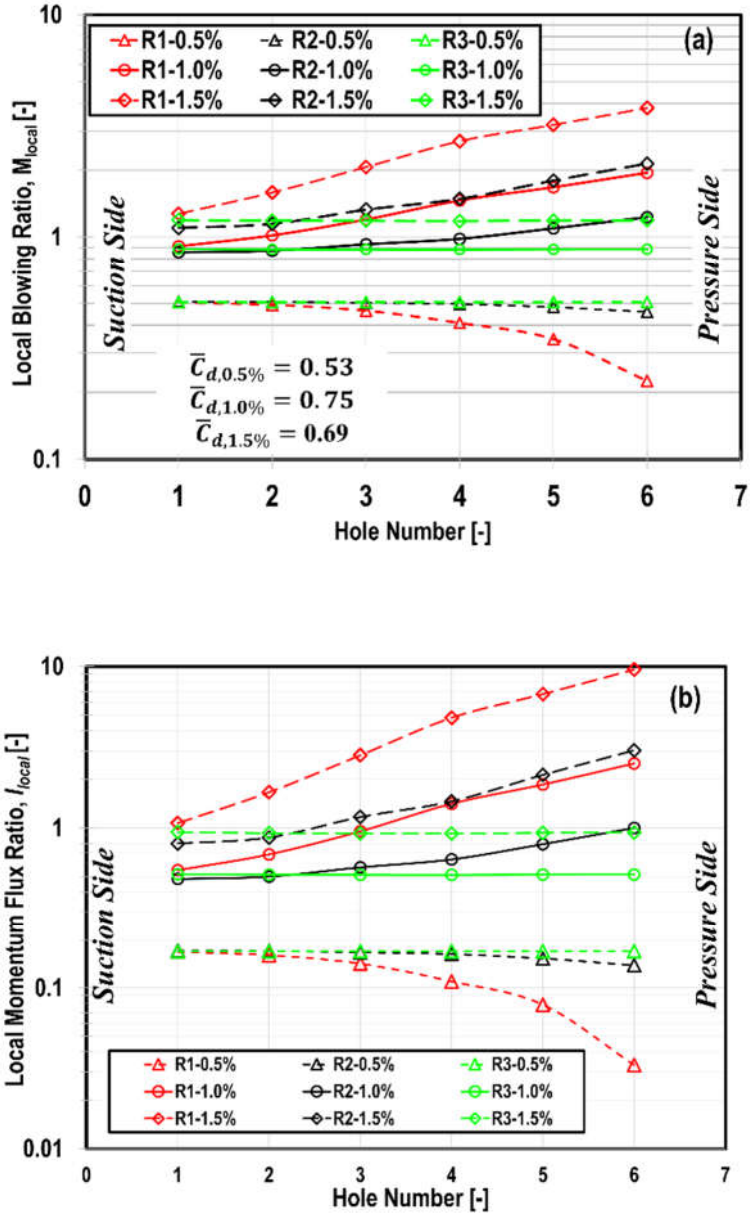

Figure 30 Local distributions of (a) blowing ratio; (b) momentum flux ratio for DR = 1.5

through the holes located in those regions**.** Somewhat counter-intuitively, however, cooling holes in those regions injects coolant at a lower blowing ratio than the holes near

the PS and downstream of the passage. As a result, The three rows (Row 1, Row 2 and Row 3), located inside the passage, are characterized by progressively decreasing values of blowing ratio that also decrease going from the pressure to the suction side of the passage. This phenomenon happens for all *MFRs*, except the lowest one as the lower blowing ratio can be found close to the PS.

Effect of Inlet Leakage MFR

Film cooling effectiveness distributions for inlet leakage are presented in **Figure 31** for all the four MFR cases while the EW MFR is set at 1.0% and *DR* = 1.5. At MFR= 0.5%, the leakage coolant provides better lateral coverage in the immediate downstream region compare to the baseline case as the blowing ratio (M = 0.76) is suitable for the cylindrical hole performance. Slight deflection of the jet is observed due to the vane flow field. The strength of the coolant decays faster due to the low momentum which readily affected by the pressure side leg of horseshoe vortex. Typically, if the coolant is injected from a region located between the saddle point and LE plane, then the cooling performance is greatly affected by the formation of the horseshoe vortex. So, in the present design, the coolant is injected from a moderate distance (X/C_{ax}= -0.38) to reduce that effect. However, the formation of horseshoe vortex still can be observed at low MFR. As MFR further goes up, the pitchwise distribution becomes more uniform, and the jet comes out at very high momentum which evidently reduces the strength of the horseshoe vortex or potentially suspends the formation of the saddle point at highest MFR. As a result, the jet can penetrate further downstream inside the passage resulting an extended coverage toward the PS similar to the results of Blair [12] and Burd et al. [15]. Overall effectiveness levels

up significantly on the entire endwall including the TE portion as the MFR increases. The leakage jet merges with the passage coolant quite well which produces a continuous and relatively uniform coverage. Moreover, downstream from the trailing edge, film effectiveness increases considerably with the MFR and feasibly covers the wake region (circled with a red line in **Figure 31**). Again, the coolant supply amount is fixed for the endwall cooling in all four cases but a careful look into the traces from Row 1 and Row 2 points to the increasing enhancement as leakage MFR increases. This is possibly due to the change in the near-wall pressure field as leakage jet weakens the secondary flows.

Figure 32 shows the corresponding pitchwise averaged film cooling effectiveness distributions. The initial two peaks in the figures are the immediate downstream of the injection locations and the valley between the peaks is due to the gap between two rows. The peaks at higher MFRs are lower than 0.5% case due to the jet lift-off which resulting in a valley right next to the second peak and recovers as soon as the coolant reattached to the surface except for MFR = 0.5%.

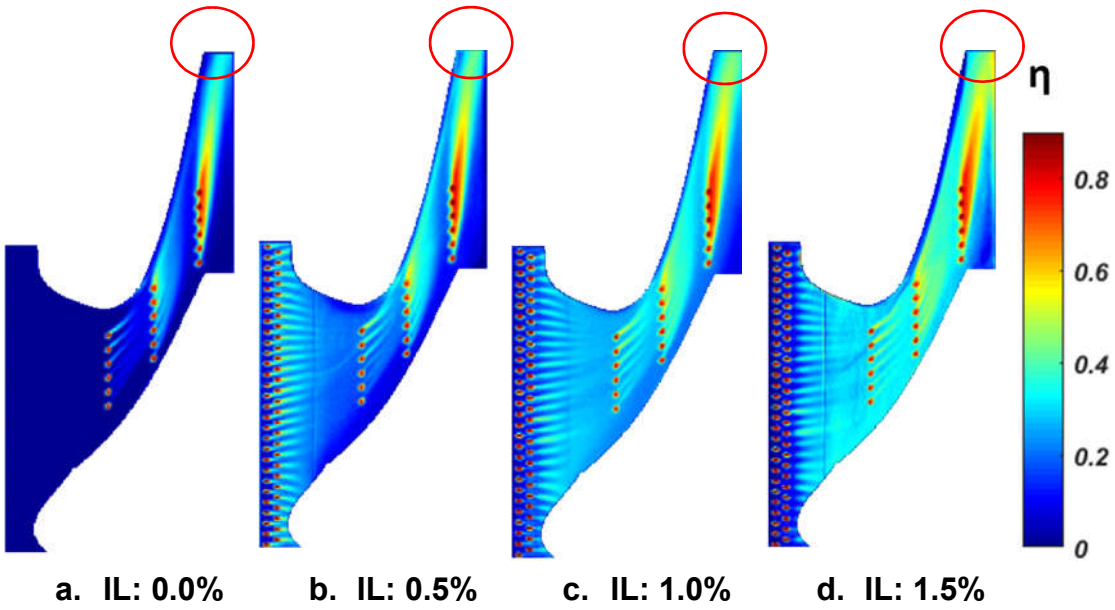

Figure 31 Film cooling effectiveness contours for all leakage MFR cases at EW MFR = 1.0% and DR = 1.5

At lower MFR (=0.5%) the effectiveness decays right downstream of the injection locations and continues as it approaches inside the passages. Then, the level goes up as soon as passage coolant is contributed from the discrete cooling holes started from X/C_{ax} = 0.3. Increasing inlet leakage flow with the fixed endwall cooling yields a substantial intensification of average cooling effectiveness for most of the part. Nevertheless, this intensification is greatly reduced right after the X/C_{ax} = 1.0. Overall, increasing leakage coolant amount has a positive effect on the endwall film cooling.

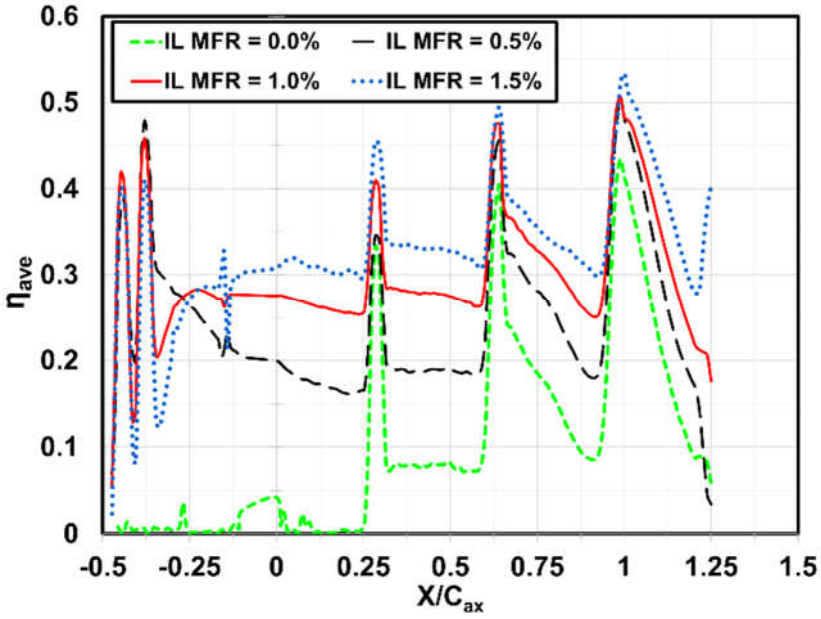

Figure 32 Pitchwise average film cooling effectiveness for all leakage MFR cases at EW MFR = 1.0% and DR = 1.5

Effect Endwall Cooling MFR

Film cooling effectiveness distributions for endwall cooling at four different coolant flow rates are presented in **Figure 33** keeping the inlet leakage MFR and density ratio at the baseline case. As the leakage injection amount is the same for all three cases then the upstream cooling behavior is expected to be the same until X/C_{ax} = 0.3 as can be seen in the contours. So, the passage cooling effect is expected to start from the beginning of Row 1.

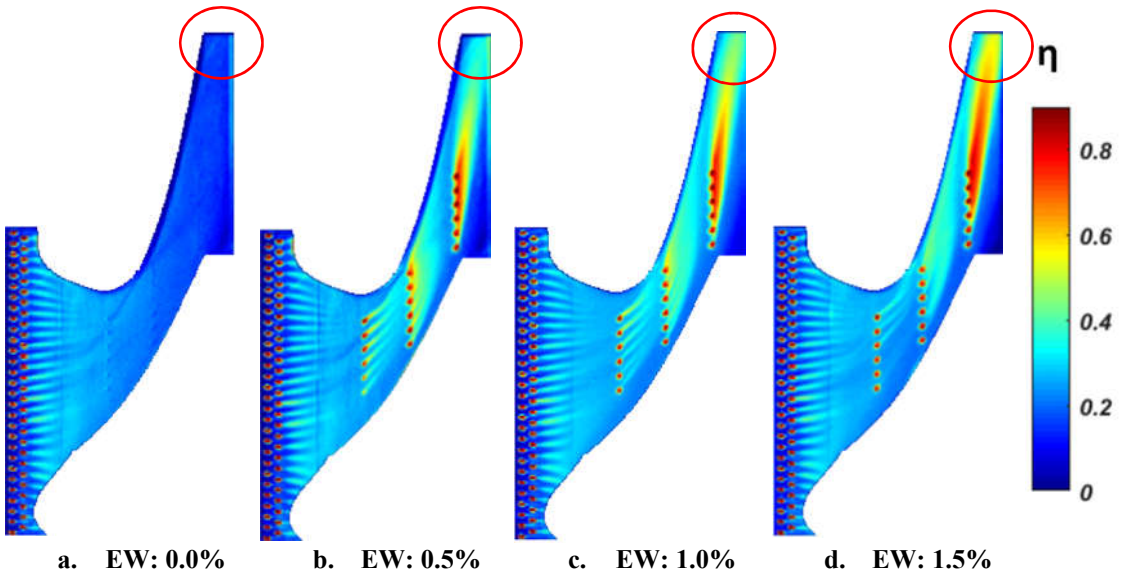

Figure 33 Film cooling effectiveness contours for all passage MFR cases at IL MFR = 1.0% and DR = 1.5

A case of no passage coolant clearly shows a very low effective zone within the passage. For low MFR (= 0.5%) case, all the holes in Row 1 contribute to the film cooling with relatively better lateral spreading over the baseline case. However, holes closer to the PS produce weak jet as expected from the lower blowing ratio indicated in **Figure 30**. As MFR increases to 1.0% case then blowing ratio gets sufficiently high for the three consecutive holes near the PS which initiate the jet lift-off tendency and reduces the downstream film protection. Further increase in the MFR to 1.5% leads to complete jet lift-off for those three holes and induces the tendency to the rest in that row as blowing rate gets remarkably high from SS to PS (refer to **Figure 30**). Coverage between Row 1 and Row 2 somewhat comparable between MFR= 0.5% and 1.0%, however, low effective zone is observed near the PS region due to the strong pressure gradient between the PS and SS. Additionally, jet turning tendency toward the potential flow-line is noticeable

rather than following the hole exit angle which is possibly dominated by the cross flow linked to the passage vortex even at higher MFR.

Coolant injected from Row 2 forms a unique cloud coverage due to the superposition of jets in a downstream location at all three MFRs but grows toward Row 3 with higher MFR. The jet trajectory from the first four holes positioned near the PS approximately trails the inviscid streamline direction while the next two holes sharply affected by the strong pressure gradient. Increasing MFR leads the holes in lift-off condition and thus the gradual change inside the cloud is diminished. As a consequence, highest MFR (=1.5%) cannot do any further improvement over the MFR = 1.0% case.

As coolant jets, marge from the holes in Row 3 at all three MFR cases, a coolant cloud similar to Row 2 but narrower in shape is observed which also extended toward the downstream. The coverage, just downstream of the row, is quite high and keep increasing as MFR grows. Furthermore, this row can effectively cool down the TE wake region (circled with red lines in **Figure 33**). Conversely, the core region would be a durability concern since it is an over-cooled zone which could lead to large gradients in endwall metal temperature and increased thermal stresses and possible higher mixing within the core may result in heat transfer augmentation. A closer look into the coolant traces gives a feel of slight overturning from the hole exit direction (indicated by black arrows) due to the cross flow effect with an indication of hole exit independency similar to the findings

of Friedrichs et al. [8]. However, this overturning could be even higher in the presence of highly turbulent flow field with no film cooling [35]. Additionally, an effective coolant coverage in the vicinity of the SS corner for all MFRs is visible which is more likely transported by the SS corner vortex.

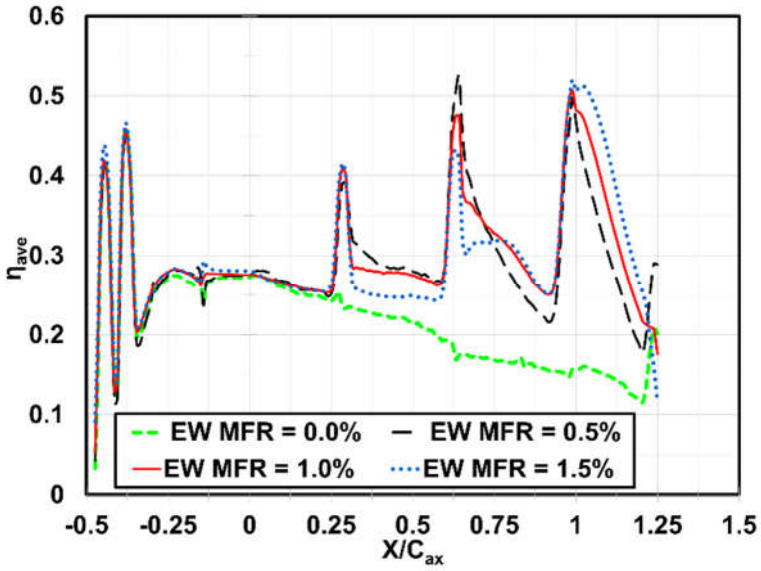

Figure 34 Pitchwise average film cooling effectiveness for all passage MFR cases at IL MFR = 1.0% and DR = 1.5

Figure 34 shows the corresponding pitchwise averaged cooling effectiveness distributions in the streamwise direction where local peaks within the passage indicate just downstream of the hole injection locations. Plots suggest that MFR 0.5% and 1.0% mostly perform better over MFR 1.5% except for the downstream region near TE.

Effect of Density Ratio

Film cooling effectiveness distributions for three different density ratios are illustrated in **Figure 35** while maintaining the flow rates in the baseline case. As the inlet leakage injection is located in a relatively uniform cross-section, then the effect of DR is similar to the results from flat plate film cooling. **Figure 35** also indicates the lateral spreading of the leakage jet which enhances systemically as DR increases. Better coolant coverage provides fairly uniform effectiveness distribution in the pitchwise direction. A low effective zone is clearly observed between holes which can be improved by reducing the distance between two rows. Jet lift-off is clearly detected for lower densities (1.0 and 1.5) at the instant downstream of the hole exits as the corresponding blowing ratio is as high as 1.48 associated with the momentum flux of 2.19 and 1.44 accordingly. Heavy density (2.0) jet stays attached to the surface due to its lower momentum, however, the jets at lower DRs re-attached to the surface and continue to provide further cooling coverage toward the passage.

But coolant from passage holes demonstrates different characteristics at different DR due to the local blowing ratio variation similar to the slashface effect study in the previous chapter. For the same blowing ratio, increase in the density ratio reduces the momentum flux of the coolant and provides better lateral coverage and inversely smaller DR retains higher momentum which susceptible to the lift-off condition.

DR effect is significantly affected by the leakage jet penetration. Due to the insufficient momentum of heavier coolant, leakage jet cannot travel that far inside the passage. Again for the same blowing ratio it already onset the jet lift-off for the lower DR (=1.0). In both cases, leakage coolant loses the strength to further penetrate within the passage resulting in continuous decay. This leaves the PS endwall region essentially unprotected as the coolant swept away by the passage cross flow. Overall, DR = 1.5 case performs better over others to achieve effective coverage over most part of the endwall.

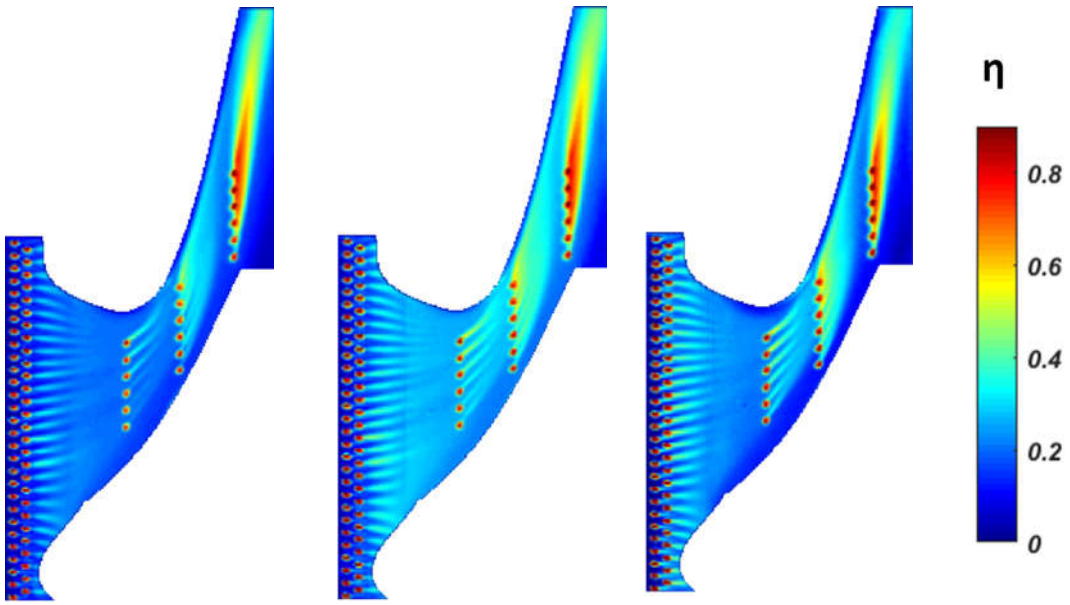

a. DR: 1.0 **b. DR: 1.5** **c. DR: 2.0**

Figure 35 Endwall Film effectiveness contours for all DR cases at IL MFR = 1.0% and EW MFR =1.0%

Line plots of pitchwise average film effectiveness for all three DRs have been presented in **Figure 36**. At the beginning, the effectiveness is higher for DR = 2.0, and steadily goes down for 1.5 and 1.0 accordingly. Then, a continuous decay region is observed for all but DR = 1.5 and 1.0 recovers as discussed. The DR 1.5 is considered to be the best case among all three DRs and then DR 2.0 over 1.0 case.

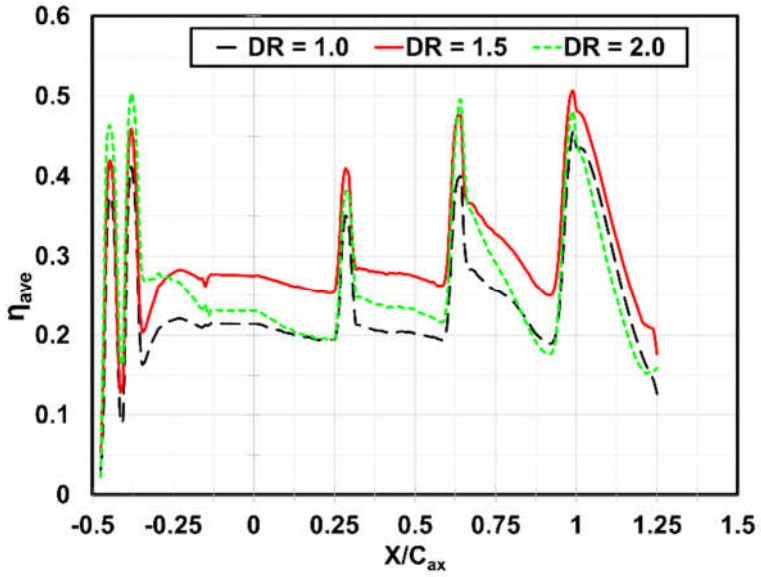

Figure 36 Pitchwise average film cooling effectiveness for all DR cases at IL MFR = 1.0% and EW MFR =1.0%

V.C.2. Cross Row (CR) Arrangement

Local Blowing Ratio Distribution

The local values of blowing ratio in each row are reported in **Figure 37** for all the EW coolant MFRs. As the leakage cooling hole rows are located at the very low-velocity zone, then average blowing ratios are considered. The corresponding values are 0.72, 1.48 and 2.22 at MFR = 0.5%, 1.0% and 1.5% accordingly. The following three rows (Row 1,

Row 2 and Row 3) are located inside the vane passage and characterized by progressively decreasing blowing ratio values towards the downstream that also decrease going from the pressure to the suction side of the passage. This happens for all MFRs, except the lowest one (in this particular condition lower blowing ratio can be found close to the PS).

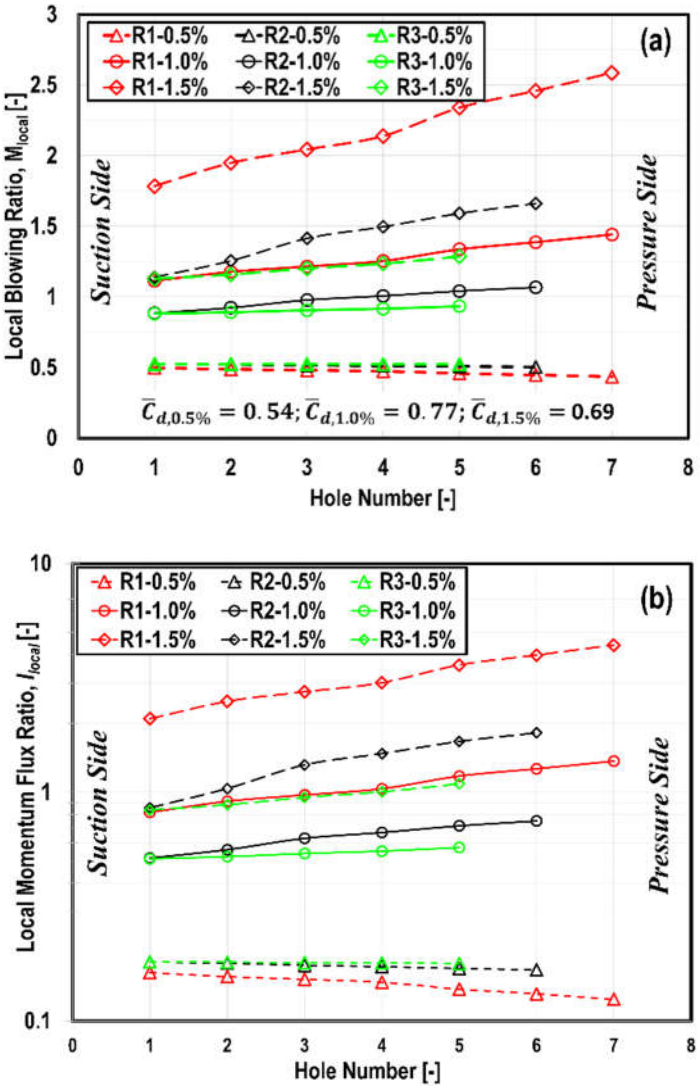

Figure 37 Local distributions of (a) blowing ratio; (b) momentum flux ratio for DR = 1.5

Effect of Endwall Coolant MFR

Film effectiveness distributions for endwall cooling at four different coolant flow rates are presented in **Figure 38** while the inlet leakage MFR and density ratio at the baseline case. As the leakage injection amount is same for all cases then the upstream cooling behavior is expected to be the same until X/C_{ax} = 0.25 as can be seen in the figure. So, the passage cooling effect is expected to start from the beginning of Row 1.

Due to the lower static pressure near the SS region as well as the downstream part of the passage (as flow accelerates) a significant higher coolant mass flux should be observed through the holes located in those regions. Somewhat counter-intuitively, however, cooling holes in those regions injects coolant at a lower blowing ratio and so lower momentum than the holes near the PS and downstream of the passage. The readers are expected to carry this unique flow physics for the rest of this section.

A case of no passage coolant is presented to just unveil the need for passage cooling and clearly shows a very low effective zone within the passage. For low MFR (=0.5%) case, coolant coverage gets better and seemed to be able to provide adequate coverage within the passage where injection from Row 1 smoothly merges with the following row and so on for Row 2. As the MFR increases to 1.0% then overall effectiveness levels up and performs better, nonetheless, initiate the lift off tendency in holes located closer to the PS as can be seen from the **Figure 38-c**. This is due to the high blowing ratio (**Figure 37**). Further increase in MFR to 1.5% causes very high blowing

ratio for Row 1 and Row 2 and results in jet lift-off from the surface where most of the jets reattached to the endwall except for the holes near the PS. As a consequence, highest MFR fails to further improve the endwall cooling compared to the BL case.

Coverage within the passage somewhat comparable for MFR= 0.5% and 1.0% at least up to X/C_{ax} = 0.9 but later part MFR = 1.0% still continue its cooling benefit. Another observation is the jet turning tendency toward the SS is dominated by the cross flow effect over the hole exit direction even at higher MFR. Moreover, the effect of so-called three-dimensional lift-off line is not evident from any of the coolant trajectories.

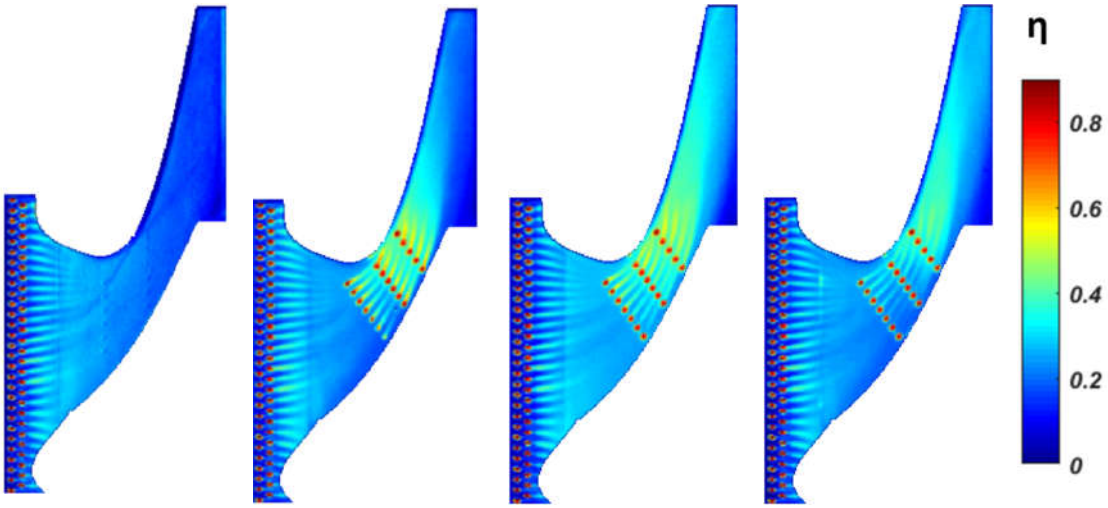

Figure 38 Film cooling effectiveness contours for all EW MFR cases at IL MFR = 1.0% and DR = 1.5

Figure 39 shows the corresponding pitchwise averaged cooling effectiveness distributions in the axial direction where local peaks indicate just downstream of the hole

injection locations. Plots show that MFR 0.5% and 1.0% mostly perform better within the passage over MFR 1.5% but as soon as the throat region is crossed MFR =1.0% gives the best result including further downstream from the TE plane. However, it is always suggested to validate the overall performance of any endwall cooling qualitatively and quantitatively, especially, when the coolant is introduced from a single supply to a complicated external flow field.

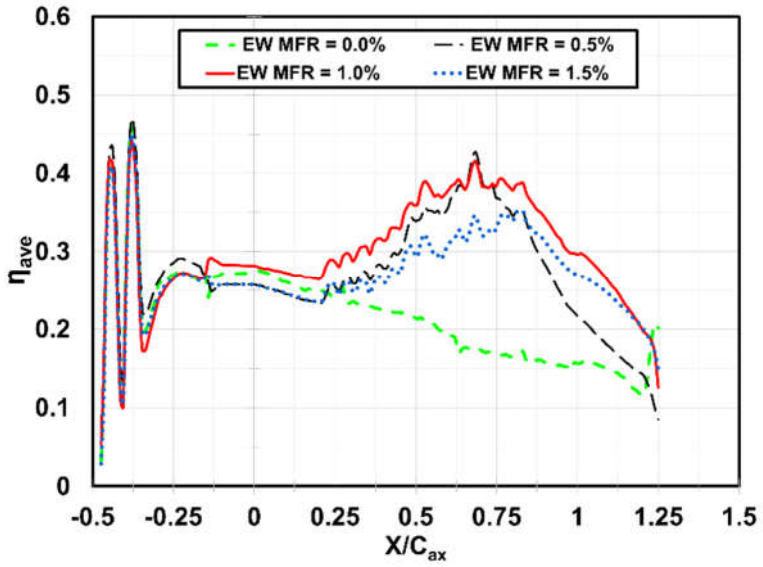

Figure 39 Pitchwise average film cooling effectiveness for all EW MFR cases at IL MFR = 1.0% and DR = 1.5

Effect of Inlet Leakage MFR

Film cooling effectiveness distributions for inlet leakage are presented in **Figure 40** for all the four MFR cases while the endwall coolant MFR is set at 1.0% and DR = 1.5. At MFR= 0.5% the leakage coolant provides better lateral spread in the immediate downstream region compare to the baseline case as the blowing ratio is suitable (M = 0.76)

for the cylindrical hole performance. As the jet comes with low momentum so slight deflection of the jet is observed due to the vane flow field and then affected by the secondary vortices. As a result, it cannot penetrate far more and swept toward the SS leaving a low effective zone near the PS region. As MFR further goes up, the pitchwise distribution becomes more uniform, and the jet comes out at very high momentum which potentially reduces the strength of the secondary flows and possibly suspends the formation of the horseshoe vortex. As a result, the jet can penetrate further downstream inside the passages with extended coverage toward the PS. Overall effectiveness levels up significantly on the entire endwall including the TE portion as the MFR increases. Conversely, further increase in the MFR up to 1.5% does not help at all as the contour looks quite identical to MFR = 1.0% except the immediate downstream of the leakage hole exits. This behavior is quite unlikely to that of AR configuration where increasing leakage amount systematically results in higher effectiveness. This clearly indicates the leakage coolant dependency on the endwall flow field which is affected by the injection of downstream cross-rows as they are distributed quite evenly over the passage. The leakage jet merges with the passage coolant quite well and produces a continuous and uniform coverage at higher MFR. Again, the coolant supply amount is fixed for the passage cooling in all four cases, but the coolant traces from all three rows indicates enhancement as leakage MFR increases and weakens the secondary flows.

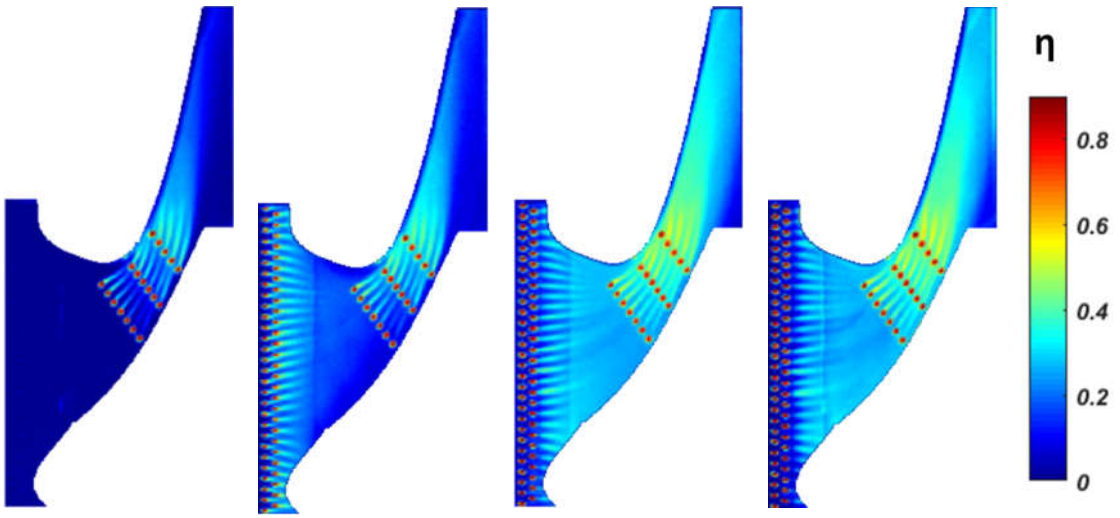

a. IL: 0.0% b. IL: 0.5% c. IL: 1.0% d. IL: 1.5%

Figure 40 Film cooling effectiveness contours for all inlet leakage MFR cases at EW MFR = 1.0% and DR = 1.5

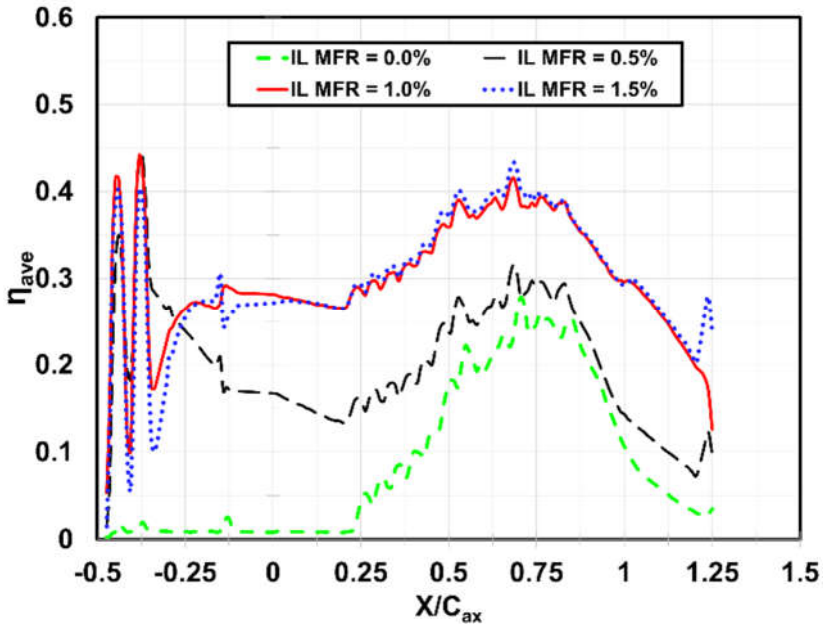

Figure 41 Pitchwise average film cooling effectiveness for all leakage MFR cases at EW MFR = 1.0% and DR = 1.5

Figure 41 shows the corresponding pitchwise averaged film cooling effectiveness distributions. The initial two peaks are the immediate downstream of the leakage coolant injection locations and the valley between the peaks is due to the gap between two rows. The peaks at higher MFRs are lower than 0.5% case due to the jet lift-off and produces a valley right next to the second peak. However, the levels start to recover as soon as the coolant reattached to the surface except for MFR = 0.5%. Then, the level gradually goes up as soon as passage coolant is contributed from the rows started from X/C_{ax} = 0.25. Increasing inlet leakage flow with fixed passage cooling yields a substantial intensification of average cooling effectiveness for most of the part. Nevertheless, this intensification is greatly reduced right after the X/C_{ax} = 1.0.

Effect of Density Ratio

Film cooling effectiveness distributions for three different density ratios are illustrated in **Figure 42** for flow rates at the baseline condition. As the leakage coolant is introduced from a uniform cross-section, lateral spreading enhances in the downstream region as DR increases similar to the results from a typical flat plate film cooling. This enhancement provides fairly uniform pitchwise effectiveness distribution for DR = 2.0. Jet lift-off is clearly detected for lower densities (1.0 and 1.5) at the instant downstream of the hole exits as the corresponding blowing is as high as 1.48 associated with the momentum flux of 1.44 and 2.19 accordingly. However, jet re-attached to the surface for both cases more or less depending on their local blowing ratios, but DR = 1.0 results in very low effectiveness distribution over the entire endwall due to the significant coolant loss into

the mainstream and leave almost an uncooled zone near the PS. Heavy density (2.0) jet stays attached to the surface due to its lower momentum which can not afford to propagate further downstream and easily affected by the strong cross flow effect (**Figure 42-c**).

Coolant traces from the passage holes indicates improved performance as DR goes up. However, overall coolant coverage is dominant by the upstream leakage jet. For the same blowing ratio, increase in the density ratio reduces the momentum of the coolant and provides better lateral coverage and inversely smaller DR retains higher momentum which is susceptible to the lift-off condition. Based on those two limiting conditions, DR =1.5 performs quite well and retains sufficient momentum to effectively travel further downstream of the passage and gives a smooth and continues coverage.

Line plots of pitchwise average film effectiveness for all three DRs have been presented in **Figure 43**. In the beginning, the effectiveness is higher for DR = 2.0, and steadily goes down for 1.5 and 1.0 accordingly. Then, a continuous decay region is observed for all but DR = 1.5 and 1.0 recovers as discussed. The DR 1.5 is considered to be the best case among all three DRs and then DR 2.0 over 1.0 case.

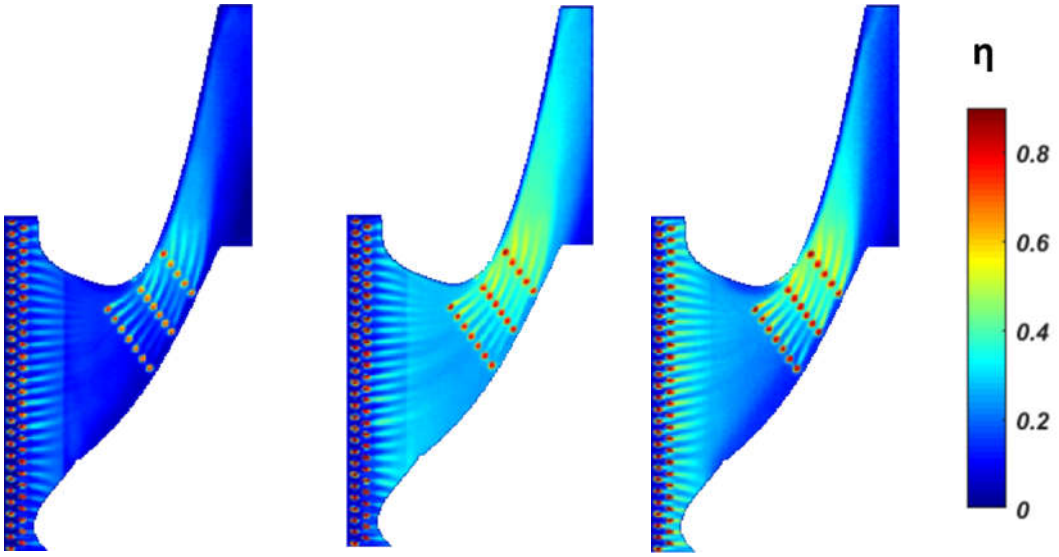

a. DR: 1.0 b. DR: 1.5 c. DR: 2.0

Figure 42 Endwall film effectiveness contours for all DR cases at IL MFR = 1.0% and EW MFR =1.0%

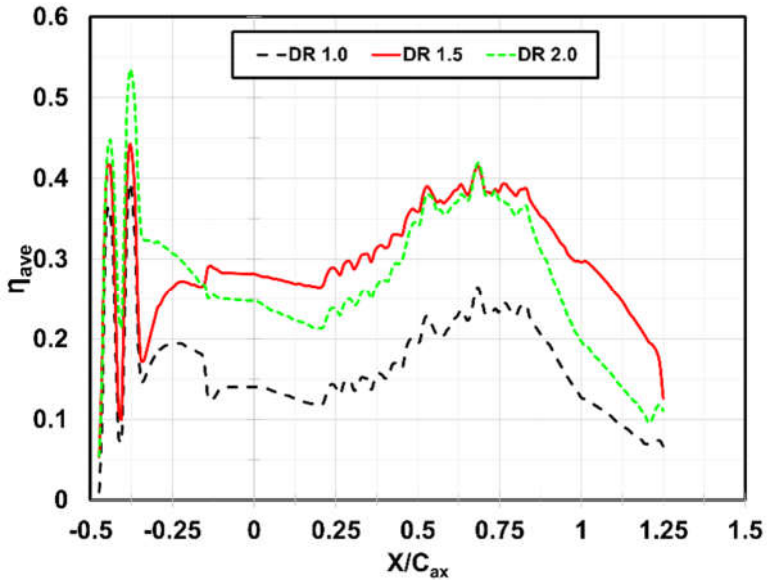

Figure 43 Pitchwise average film cooling effectiveness for all DR cases at IL MFR = 1.0% and EW MFR =1.0%

Comparison between AR and CR Configurations

A fair comparison is carried out between the AR and CR configurations in **Figure 44**. This assessment is quite valid as hole numbers and geometries are all same on both designs except the hole locations. Both configurations are capable of providing good coverage. AR configuration is exposed to the overcooled region after the third row while this is diluted by a gradual change in CR configuration and provides fairly uniform effectiveness level. The gradual change in the effectiveness possibly accountant for the reduced aerodynamic loss as less mixing is expected. CR configuration provides weaker coverage toward the TE region than that of the AR configuration. Cooling holes in CR configuration are relatively closer to the PS compare to the AR one which also provides better coverage in that area.

The pitchwise average comparison in **Figure 45** shows that effectiveness increases steadily for the CR configuration and then decreases in the similar fashion while AR one has very high peaks and then a quick drop. From the design point of view, the steady growth is expected. Otherwise, it may lead to a large gradient of metal temperatures which increase thermal stresses and would be a durability concern.

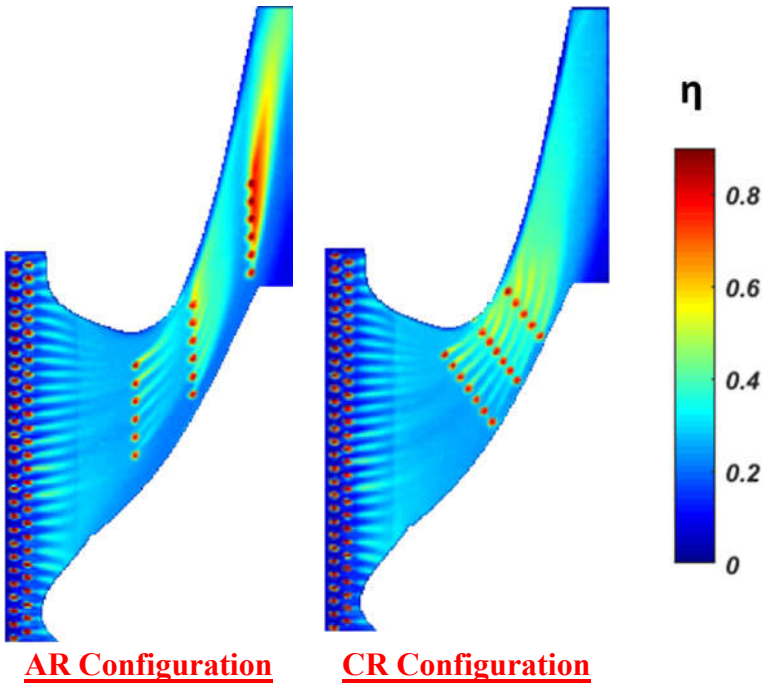

Figure 44 Film cooling effectiveness contours for the baseline case at EW MFR= 1.0%, IL MFR = 1.0% and DR = 1.5

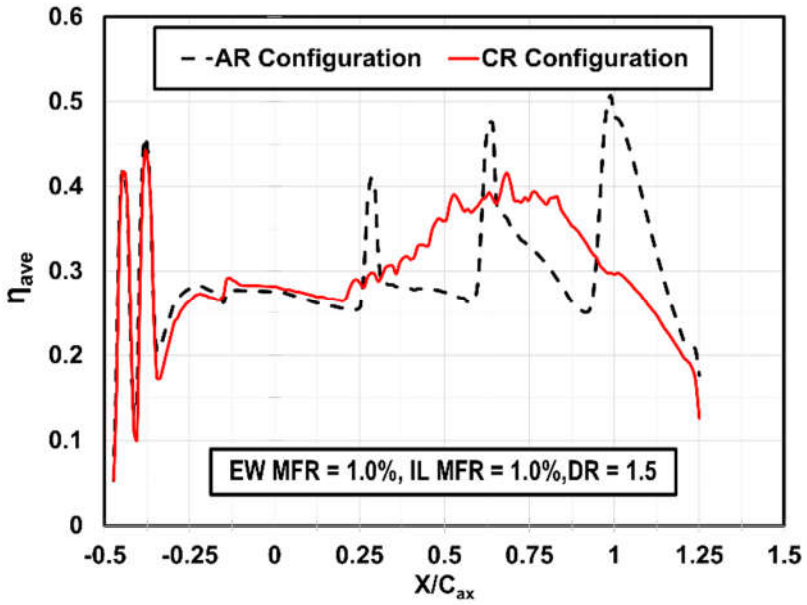

Figure 45 Pitchwise average film effectiveness distribution for AR and CR configurations baseline case at EW MFR= 1.0%, IL MFR = 1.0% and DR = 1.5

Area-averaged Film Cooling Effectiveness

To quantify the film cooling benefit for the entire endwall surface, area-averaged values of adiabatic film cooling effectiveness were estimated for all cases, and values are shown in **Figure 46**. The area covers one full passage beginning at the first row of the upstream leakage simulator (X/C_{ax} = -0.47) to the X/C_{ax} = 1.25. The performance of the baseline case for CR configuration is found to be the best for DR and MFR variation.

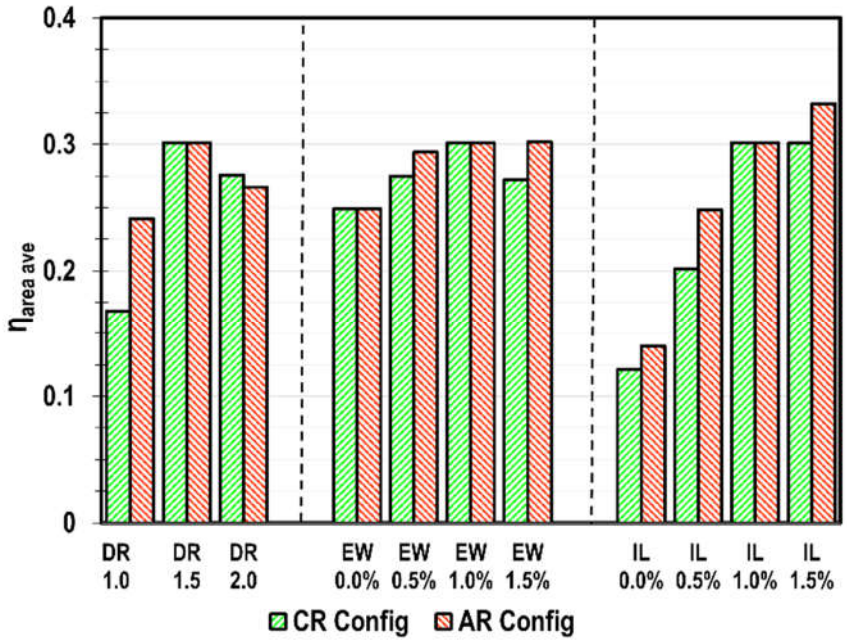

Figure 46 Area-averaged film cooling effectiveness for all cases

Additionally, a comprehensive comparison is made with the AR configuration where the baseline case values found to be quite close for both configurations while the higher value for DR = 2.0 is observed for CR configuration over the AR one. However, AR

arrangement shows monotonic growth as leakage MFR goes up which is unlikely for this CR configuration.

In general, AR configuration mostly performs slightly better than the CR one and CR configuration provides overall better uniformity (**Figures 44 and 45**). As a result, both are comparable designs. However, CR configuration is easier to refine and can be further improved by shifting hole/holes from Row 2/Row 3 while increasing the hole-to-hole spacing.

V.C.3. Cluster Arrangements

Local Blowing Ratio Distribution

The local blowing ratio of each group is reported in **Figure 47** for all the EW coolant MFRs. As the leakage cooling holes are located at the very low-velocity zone, then the average blowing ratios are considered. The corresponding values are 0.72, 1.48 and 2.22 at MFR = 0.5%, 1.0% and 1.5% accordingly. The following groups (G1~ G4 for cluster A and G1~ G6 for cluster B) are located inside the vane passage and characterized by progressively decreasing blowing ratio towards the downstream that also decreases going from the pressure to the suction side of the passage. This happens for all MFRs, except the lowest one (in this particular condition lower blowing ratio (less than 1) can be found close to the PS).

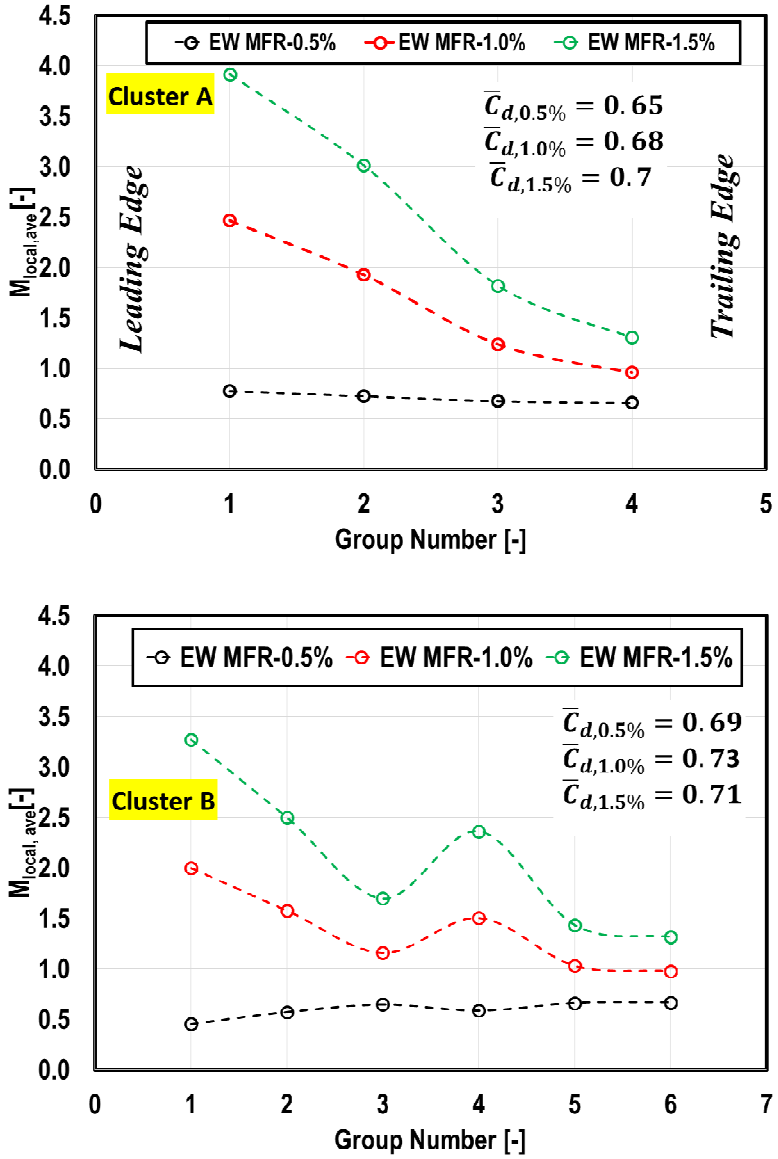

Figure 47 Local blowing ratio distributions for Cluster A and Cluster B

V.C.3.2. Effect of Endwall Coolant MFR

Film effectiveness distributions for endwall cooling at four different coolant flow rates are presented in **Figure 48** while the inlet leakage MFR and density ratio at the baseline case. As the leakage injection amount is same for all cases, then the upstream cooling

behavior is expected to be the same until X/Cax = 0.25 as can be seen in **Figure 48**. So, the passage cooling effect is expected to start from the beginning of G1 for cluster A and G1~ G3 for cluster B.

For low MFR (= 0.5%) case, coolant coverage is better for both designs, however, cluster B only able to provide adequate coverage within the passage. Coolant jets are expected to spread towards the suction side at low MFR due to the cross-flow effect. Cluster B responds to that effect quite significantly while in cluster A coolant just tries to follow the PS curve and creates continuous coverage. Increasing MFR increases to 1.0% initiate the lift-off tendency located closer to the PS near LE zone due to the high blowing ratios (refer to **Figure 47**). Further increase in MFR to 1.5% results in extremely high blowing ratio for G1 and G2 in cluster A and G1, G2 and G4 in cluster B which onset the jet lift-off from the surface with minimum jet reattached. As a consequence, highest MFR fails to further improve the endwall cooling. Another observation is the downstream cooling gets better with the increasing MFR for both designs.

Figure 49 shows the corresponding pitchwise averaged cooling effectiveness distributions in the axial direction where local peaks indicate just downstream of the hole injection locations. Plots show that MFR 0.5% and 1.0% mostly perform better within the passage over MFR 1.5% but as soon as the throat region is crossed MFR =1.0% gives the best result including further downstream from the TE plane.

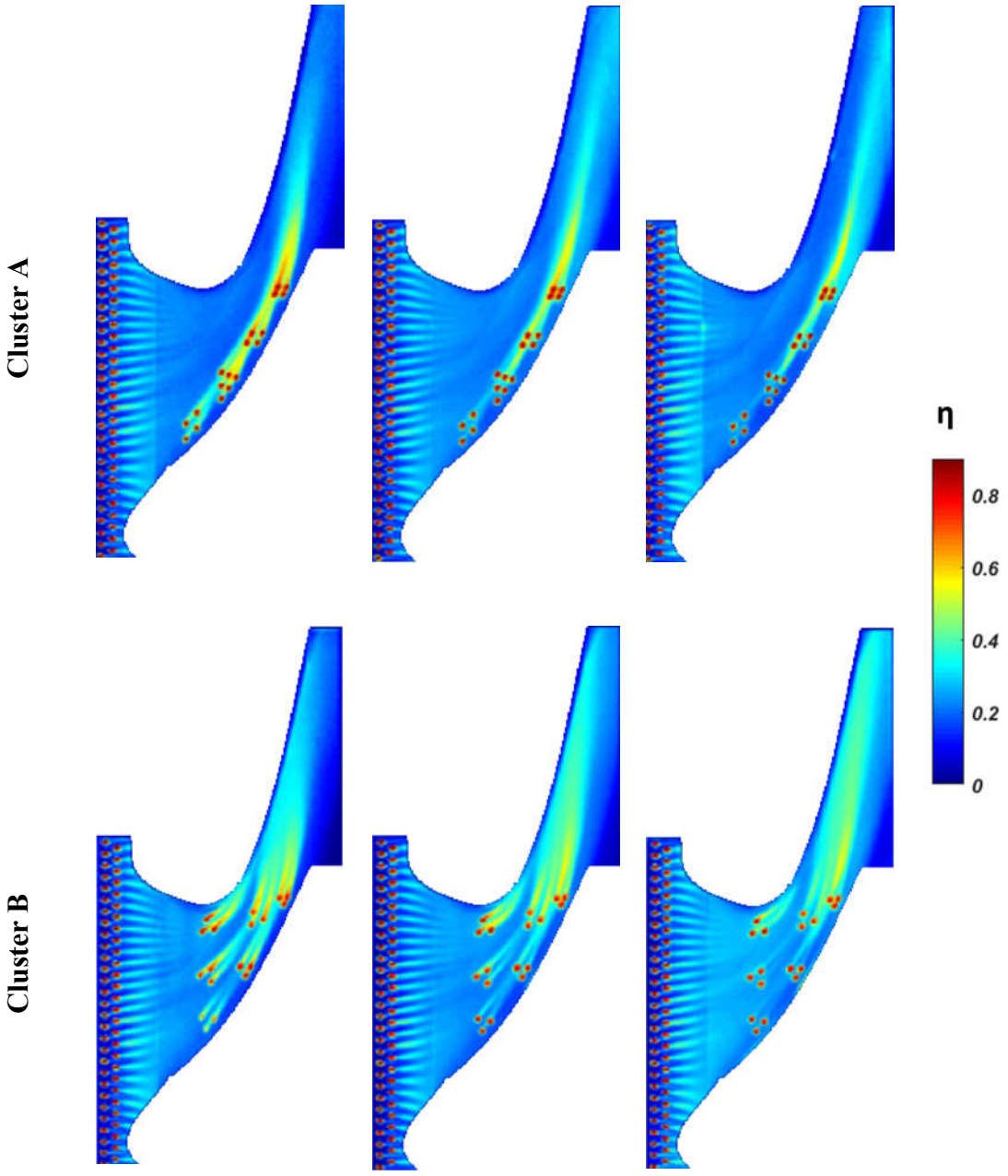

Figure 48 Film cooling effectiveness contours for all EW MFR cases at IL MFR = 1.0% and DR = 1.5

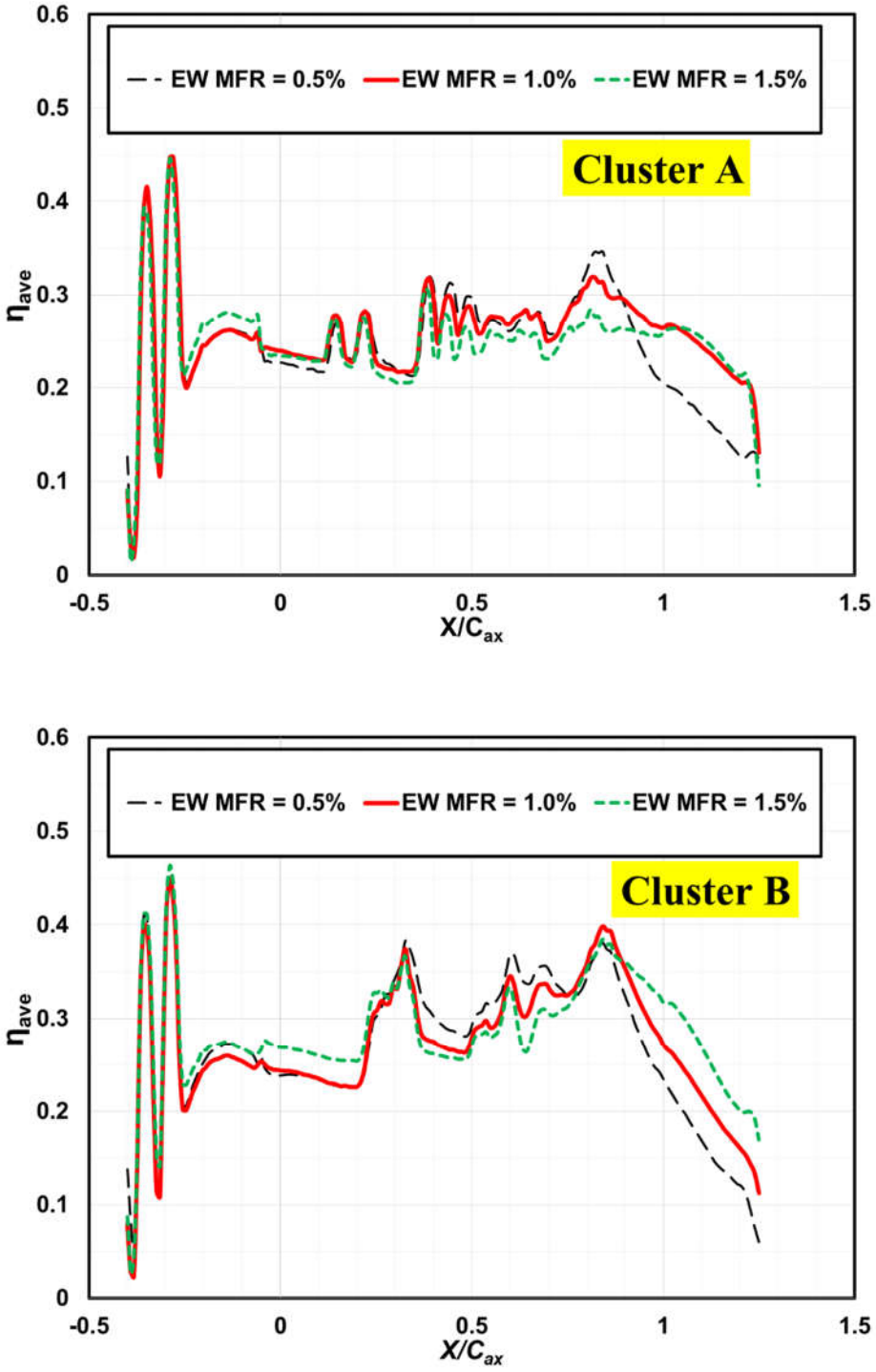

Figure 49 Pitchwise average film cooling effectiveness for all EW MFR cases at IL MFR = 1.0% and DR = 1.5

Effect of Inlet Leakage MFR

Film cooling effectiveness distributions for inlet leakage are presented in **Figure 50** for all the four MFR cases while the endwall coolant MFR is set at 1.0% and DR = 1.5. At MFR= 0.5% the leakage coolant provides better lateral spread in the immediate downstream region compare to the baseline case as the blowing ratio is suitable (M = 0.76) for the cylindrical hole performance. As the jet comes with low momentum so slight deflection of the jet is observed due to the vane flow field and then affected by the secondary vortices. As a result, it cannot penetrate far more and swept toward the SS leaving a low effective zone near the PS region. As MFR further goes up, the pitchwise distribution becomes more uniform, and the jet comes out at very high momentum which potentially reduces the strength of the secondary flows and possibly suspends the formation of the horseshoe vortex. As a result, the jet can penetrate further downstream inside the passages with extended coverage toward the PS. Overall effectiveness levels up significantly on the entire endwall including the TE portion as the MFR increases. Further increase in the MFR up to 1.5% systematically results in higher effectiveness. Additionally, the leakage coolant jet also enhances the downstream endwall cooling performance as due to change in the endwall flow field. Overall, the leakage jet merges with the passage coolant quite well for cluster B and produces a continuous and relatively uniform coverage at the higher MFR.

Figure 51 shows the corresponding pitchwise averaged film cooling effectiveness distributions. The initial two peaks are the immediate downstream of the leakage coolant

injection locations and the valley between the peaks is due to the gap between two rows. The peaks at higher MFRs are lower than 0.5% case due to the jet lift-off and produces a

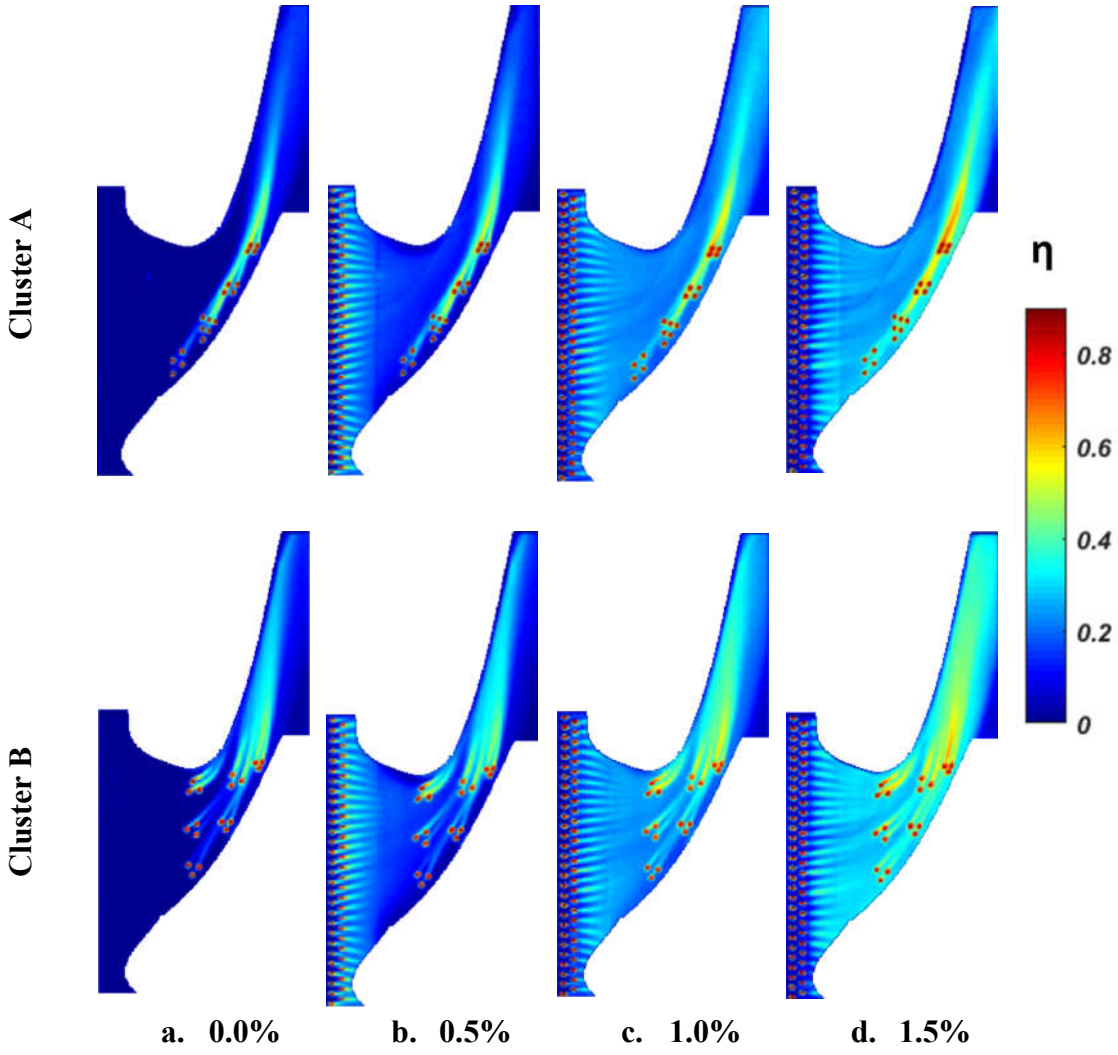

Figure 50 Film cooling effectiveness contours for all IL MFR cases at EW MFR = 1.0% and DR = 1.5

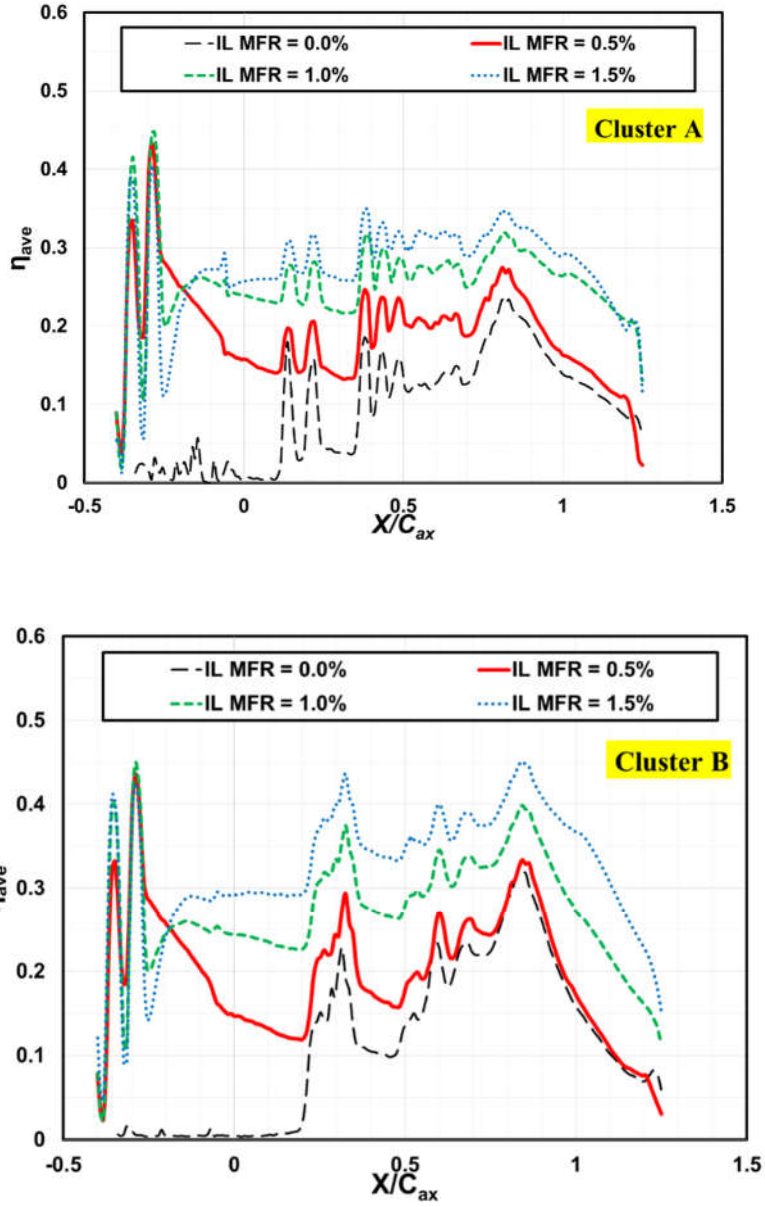

Figure 51 Pitchwise average film cooling effectiveness for all leakage MFR cases at EW MFR = 1.0% and DR = 1.5

valley right next to the second peak. However, the levels start to recover as soon as the coolant reattached to the surface except for MFR = 0.5%. Then, the level gradually goes up as soon as passage coolant is contributed from the rows started from X/C_{ax} = 0.25.

Increasing inlet leakage flow with fixed passage cooling yields a substantial intensification of average cooling effectiveness for most of the part. Nevertheless, this intensification is greatly reduced right after the X/C_{ax} = 1.0.

Effect of Density Ratio

Film cooling effectiveness distributions for three different density ratios are illustrated in **Figure 52** for flow rates at the baseline condition. As the leakage coolant is introduced from a uniform cross-section, lateral spreading enhances in that region as DR increases identical to the results from a typical flat plate film cooling. This enhancement provides fairly uniform pitchwise effectiveness distribution for DR = 2.0. Jet lift-off is clearly detected for lower densities (1.0 and 1.5) at the instant downstream of the hole exits as the corresponding blowing is as high as 1.48. However, coolant jet is re-attached to the surface for both cases more or less depending on their local blowing ratios but DR = 1.0 results in very low effectiveness distribution over the entire endwall due to the significant coolant loss into the mainstream and leave almost an uncooled zone near the PS. Heavy density (2.0) jet stays attached to the surface due to its lower momentum which cannot afford to propagate further downstream and easily affected by the strong cross flow effect (**Figure 52-c**).

Coolant traces from the passage holes indicates improved performance as DR goes up. However, overall coolant coverage is dominant by the upstream leakage jet. For the same blowing ratio, increase in the density ratio reduces the momentum of the coolant and

provides better lateral coverage and inversely smaller DR retains higher momentum which is susceptible to the lift-off condition. Based on those two limiting conditions, DR =1.5 performs quite well and retains sufficient momentum to effectively travel further downstream of the passage and gives a smooth and continues coverage.

Line plots of pitchwise average film effectiveness for all three DRs have been presented in **Figure 53**. In the beginning, the effectiveness is higher for DR = 2.0 and steadily goes down for 1.5 and 1.0 accordingly. Then, a continuous decay region is observed for all but DR = 1.5 and 1.0 recovers as discussed. The DR 1.5 is considered to be the best case among all three DRs and then DR 2.0 over 1.0 case.

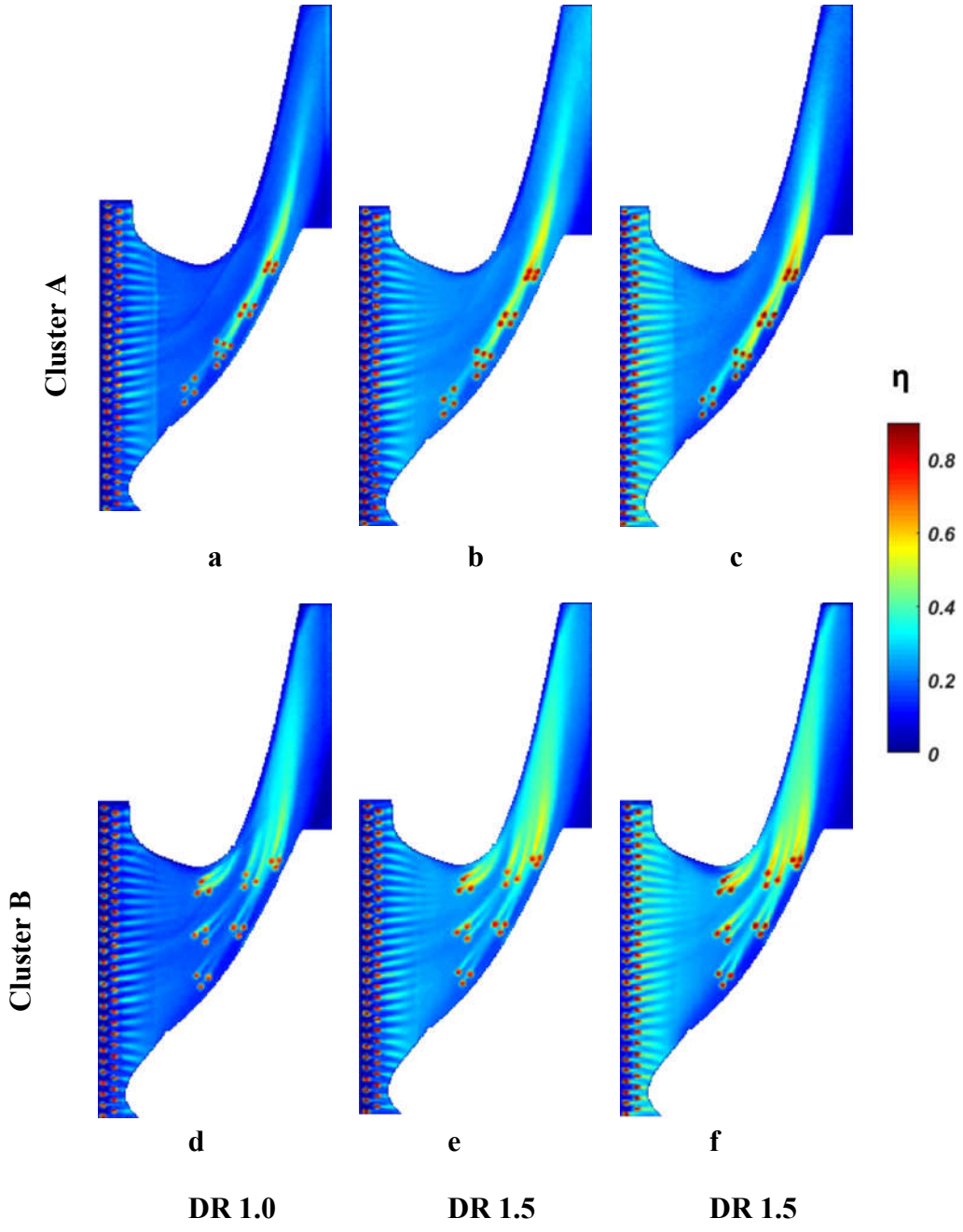

Figure 52 Endwall Film effectiveness contours for all DR cases at IL MFR = 1.0% and EW MFR =1.0%

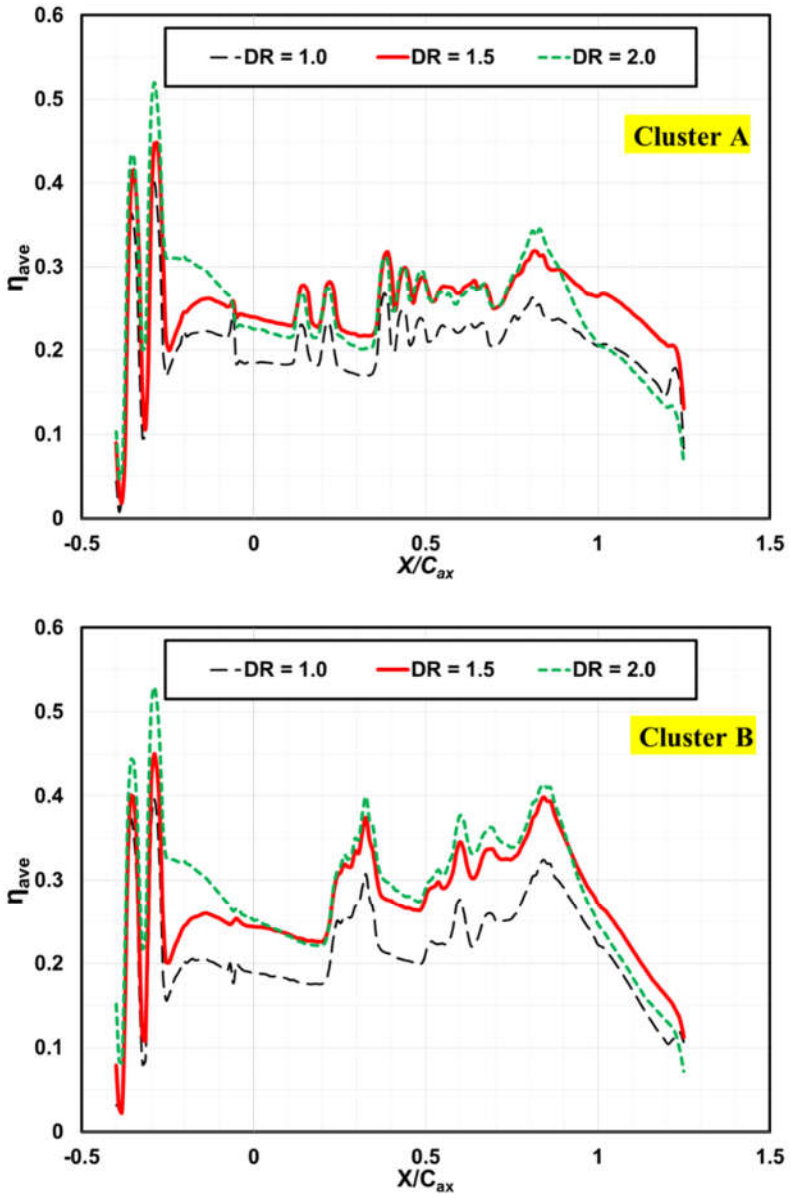

Figure 53 Pitchwise average film cooling effectiveness for all DR cases at IL MFR = 1.0% and EW MFR =1.0%

Area-averaged Film Cooling Effectiveness

To quantify the film cooling benefit for the entire endwall surface, area-averaged values of adiabatic film cooling effectiveness were estimated for all cases, and values are

shown in **Figure 54**. The area covers one full passage beginning at the first row of the upstream leakage simulator (X/C_{ax} = -0.47) to the X/C_{ax} = 1.25. The performance of the baseline case for cluster B configuration is found to be the best and shows monotonic growth in any case. For cluster A configuration the baseline case values found to be the best cases based on DR and EW MFR.

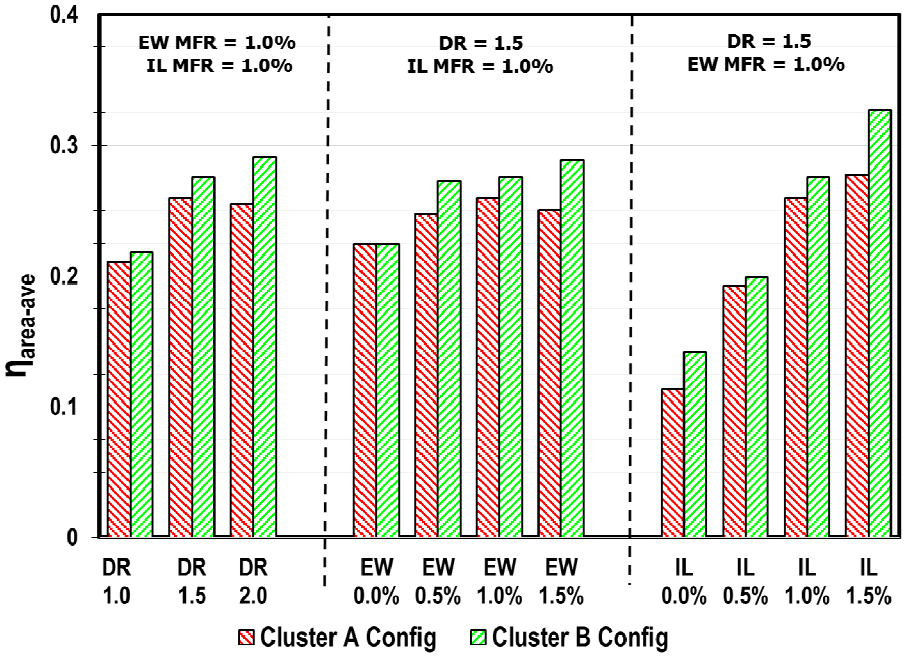

Figure 54 Area-averaged film cooling effectiveness for all cases

V.D OVERALL COMPARISON

The contours of four configurations are compared side by side in **Figure 55** at the baseline case. Obviously, AR, CR and cluster B found to have higher effectiveness over cluster A. However, CR and cluster B provides relatively uniform coverage on the overall

endwall. The pitchwise average is also represented in **Figure 56** where CR arrangement is showing better distribution along the axial distance. **Figure 57** is showing the area-average film cooling effectiveness. AR and CR configurations are found to have the highest values over cluster A and cluster B.

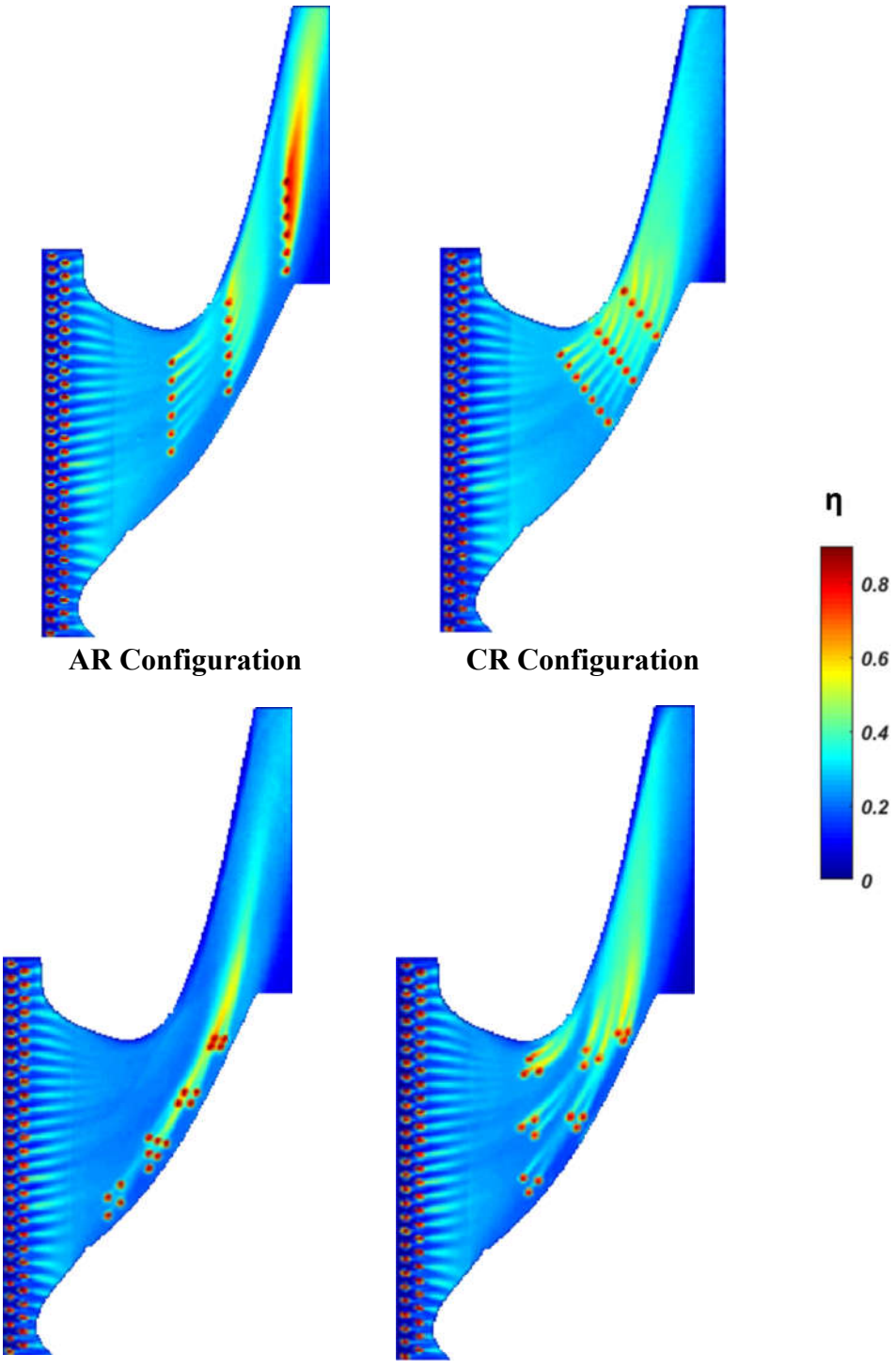

Figure 55 Film cooling effectiveness contours for all four designs at the baseline condition (EW MFR 1.0%; IL MFR 1.5%; DR 1.5)

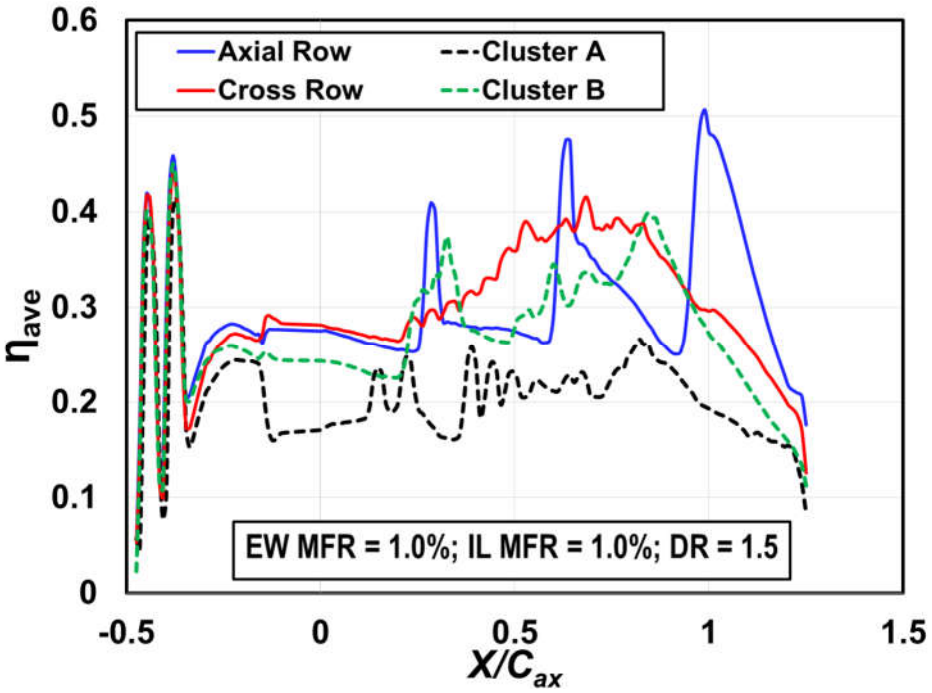

Figure 56 Pitchwise average film cooling effectiveness for all four designs at the baseline case

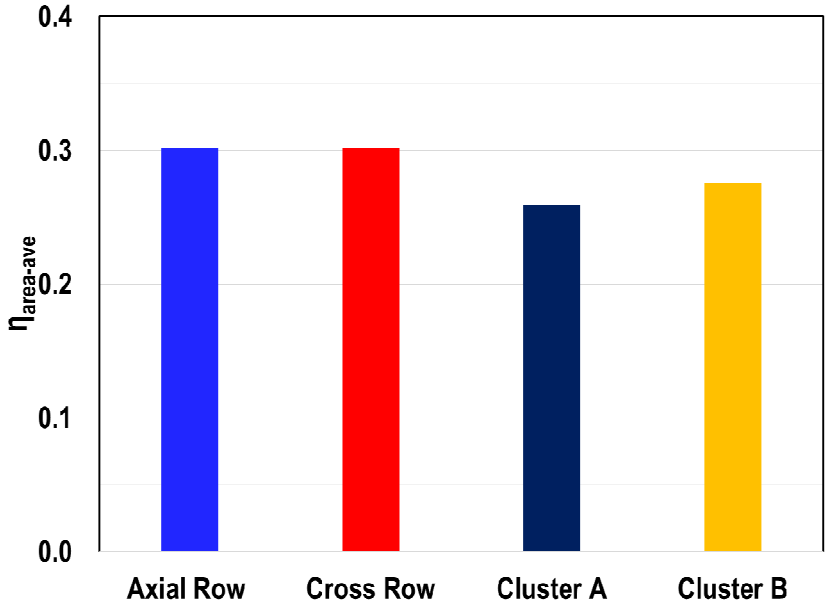

Figure 57 Area-averaged film cooling effectiveness for all four designs at the baseline case

CHAPTER VI

CONCLUSIONS

In the gas turbine cooling technology, film cooling is an active cooling scheme to protect the external surfaces those are exposed to hot gas paths. Turbine vane endwall surface is one of the critical regions where achieving an effective and uniform film cooling is very difficult and also challenging due to the presence of various vortices and pressure gradients. Thus, a detailed knowledge of the endwall film cooling is necessary which potentially reduces the strength of those vortices and offers better cooling coverage with the optimum amount of coolant.

VI.A SLASHFACE EFFECT ON ENDWALL FILM COOLING

Film cooling effectiveness distributions on the turbine vane endwall surface associated to various leakage flows and discrete film cooling holes were measured using the PSP technique in a scaled vane cascade. The study was conducted for discrete film cooling holes including leakage flows from the combustor-vane endwall gap and slashface gap. The inlet leakage flow was simulated by two rows of staggered cylindrical holes to cool down the upstream portion of the endwall. And slashface was simulated within one of the two passages. Two-dimensional film cooling effectiveness distributions and pitchwise averaged effectiveness distributions on the endwall surfaces were presented and discussed for the variation of mass flow ratio (MFR) and density ratio (DR). Then, comparisons

were made with the baseline case for the individual cooling feature. The major findings can be summarized below:

1. For inlet leakage injection, endwall surface film cooling effectiveness increases with the mass flow ratios and offers extended coverage toward the pressure side and travel further downstream of the passage. It also results in uniform pitchwise coolant distribution in the frontal part of the endwall with higher MFR.
2. For slashface leakage, a significant amount of coolant tends to exit from the downstream portion (near the throat) of the gap due to mainstream flow acceleration and shows higher effectiveness level. However, at very higher MFR, coolant comes out of the upstream portion spill off toward the pressure side. It is possibly due to the mixing of slashface coolant with mainstream flow.
3. For discrete film cooling, the result also shows an increase in the magnitude of effectiveness at larger MFR. However, for passage without slashface, further increases in the mass flow from baseline case shows a minor improvement, which indicates an optimum condition for this particular design.
4. Increasing density ratio is effective for upstream of the endwall but for the slashface and discrete film cooling holes it is not that significant due to the relatively low blowing ratio.

VI.B ENDWALL FILM COOLING FROM VARIOUS DFC CONFIGURATIONS

Endwall film cooling is investigated for a full coverage passage cooling design including upstream inlet leakage flow using the PSP technique. The leakage flow was

simulated by two rows of staggered cylindrical holes with a very high-velocity ratio (= 1). Two-dimensional film cooling effectiveness distributions on the endwall surface and pitchwise averaged effectiveness along the axial distance were presented and discussed for the variation of the mass flow ratio (MFR) and density ratio (DR). The major findings are summarized below:

1. For endwall cooling, the results mostly show insignificant increase in the magnitude of effectiveness at higher MFR. Based on the reduced coolant requirement, the lower value of MFR 1.0% may be considered as the best condition with better coverage for any configuration.

2. For the inlet leakage injection, cooling effectiveness increases systematically as the MFR goes up and exhibits extended coverage toward the pressure side and further downstream of the passage. Pitchwise uniformity of the coolant distribution is achieved on the frontal part of the endwall at higher MFR. Higher MFR also help to enhance the downstream cooling performance. But in CR design, this benefit is limited by the downstream coolant injection which creates a blockage to the leakage jet. Additionally, leakage jet significantly reduces the strength of the horseshoe vortex and corresponding passage vortex which enhances the overall endwall cooling performance.

3. Increasing density ratio performs better in the upstream of endwall region but behaves differently within the passage due to the local changes in the coolant momentum. Overall, DR = 1.5 mostly performs better.

4. Between AR and CR, the AR design and between Cluster A and Cluster B, cluster B can provide relatively higher effectiveness with better coverage.

Finally, a higher level of effectiveness with a better coverage is always expected but it also promotes additional concerns such as corresponding heat transfer augmentation and aerodynamic loss penalty. Thus, further investigation with the inclusion of heat transfer and loss measurement should be able to confirm the overall performance of the endwall cooling.

REFERENCES

[1] Han, J. C., Dutta, S., and Ekkad, S., 2012, "Gas Turbine Heat Transfer and Cooling Technology," CRC Press, Taylor & Francis Group, Florida.

[2] Langston, L.S., Nice, L.M., and Hooper, R.M., 1976, "Three- Dimensional Flow within a Turbine Cascade Passage," ASME Paper No. 76-GT-50.

[3] Langston, L.S., 1980, "Crossflows in a Turbine Cascade Passage," J. Engineering for Power, 102, pp. 866-874. 145.

[4] Sharma O.P., Butler T.L., 1987, "Prediction of endwall losses and secondary flows in axial flow turbine cascades," ASME J. Turbomach., 109, pp. 229-236.

[5] Goldstein, R.J. and Spores, R.A., 1988, "Turbulent Transport on the Endwall in the Region between Adjacent Turbine Blades." ASME J. Heat Transfer, 110, pp. 862-869.

[6] Takeishi, K., Matsuura, M., Aoki, S., and Sato, T., 1990, "An Experimental Study of Heat Transfer and Film Cooling on Low Aspect Ratio Turbine Nozzles," ASME J. Turbomach., 112(3), pp. 488-496.

[7] Harasgama, S.P. and Burton, C.S., 1992, "Film Cooling Research on the Endwall of a Turbine Nozzle Guide Vane in a Short Duration Annular Cascade: Part 1 – Experimental Technique and Results," ASME J. Turbomach., 114, pp. 734-740.

[8] Friedrichs, S., Hodson, H.P., and Dawes, W.N., 1996, "Distribution of Film-Cooling Effectiveness on a Turbine Endwall Measured Using the Ammonia and Diazo Technique," ASME J. Turbomach., 118, pp. 613-621.

[9] Friedrichs, S., Hodson, H.P., and Dawes, W.N., 1997, "Aerodynamic Aspects of Endwall Film Cooling," ASME J. Turbomach., 119, pp. 786-793.

[10] Friedrichs, S., Hodson, H.P., and Dawes, W.N., 1998, "The Design of an Improved Endwall Film Cooling Configuration," ASME Paper No. 98-GT-483.

[11] Barigozzi, G., Benzoni, G., Franchini, G., and Derdichizzi, A., 2005, "Fan-Shaped Hole Effects on the Aero-Thermal Performance of a Film-Cooled Endwall," ASME Paper No. GT2005-68544.

[12] Blair, M.F., 1974, "An Experimental Study of Heat Transfer and Film Cooling on Large-Scale Turbine Endwall," ASME J. Heat Transfer, 96, pp. 524-529.

[13] Granser, D. and Schulenberg, T., 1990, "Prediction and Measurement of Film Cooling Effectiveness for a First-Stage Turbine Vane Shroud," ASME Paper No. 90-GT-95.

[14] Burd, S. W., and Simon, T. W., 2000, "Effects of Slot Bleed Injection Over a Contoured Endwall on Nozzle Guide Vane Cooling Performance: Part I: Flow Field Measurements," ASME Paper No. 2000-GT-199.

[15] Burd, S. W., Satterness, C. J., and Simon, T. W., 2000. "Effects of Slot Bleed Injection Over a Contoured Endwall on Nozzle Guide Vane Cooling Performance: Part II: Thermal Measurements". ASME Paper No. 2000-GT-200.

[16] Oke, R., Simon, T., Shih, T., Zhu, B., Lin, Y. L., and Chyu, M., 2001. “Measurements Over a Film-Cooled, Contoured Endwall with Various Coolant Injection Rates”. 2001-GT-140.

[17] Oke, R., and Simon, T., 2002, “Film-Cooling Experiments with Flow Introduced Upstream of a First Stage Nozzle Guide Vane Through Slots of Various Geometries,” ASME Paper No. GT2002-30169.

[18] Lynch SP, Thole K. A., 2008 “The Effect of Combustor-Turbine Interface Gap Leakage on the Endwall Heat Transfer for a Nozzle Guide Vane,” ASME J. Turbomach., 130(4), 041019.

[19] Liu, G., Liu, S., Zhu, H., Lapworth, B.C., and Forest, A.E., 2004, “Endwall Heat Transfer and Film Cooling Measurements in a Turbine Cascade with Injection Upstream of Leading Edge,” Heat Transfer–Asian Research, 33, pp. 141-152.

[20] Oke, R., Simon, T. W., Burd, S. W., and Vahlberg, R., 2000, “Measurements in a Turbine Cascade Over a Contoured Endwall: Discrete Hole Injection of Bleed Flow,” 2000-GT-0214.

[21] Zhang, L.J. and Jaiswal, R.S., 2001, “Turbine Nozzle Endwall Film Cooling Study Using Pressure-Sensitive Paint,” ASME J. Turbomach., 123, pp. 730-735.

[22] Zhang, L.J. and Moon, H.K., 2003, “Turbine Nozzle Endwall Inlet Film Cooling–The Effect of a Backward Facing Step,” ASME Paper No. GT2003-38319.

[23] Zhang, L.J., Yin, J., Liu, K., and Moon, H. K., 2015, "Effect of Hole Diameter on Nozzle Endwall Film Cooling and Associated Phantom Cooling," ASME Paper No. GT2015-42541.

[24] Knost, D.G. and Thole, K.A., 2004, "Adiabatic Effectiveness Measurements of Endwall Film Cooling for a First Stage Vane," ASME Paper No. GT2004-53326.

[25] Aunapu, N. V., Volino, R. J., Flack, K. A., and Stoddard, R. M., 2000, "Secondary Flow Measurements in a Turbine Passage With Endwall Flow Modification," ASME J. Turbomach. 122(4), pp. 651-658.

[26] Reid, K., Denton, J., Pullan, G., Curtis, E., and Longley, J., "The Interaction of Turbine Inter-Platform Leakage Flow With the Mainstream Flow," ASME Paper No. GT2005-68151.

[27] Reid, K., Denton, J., Pullan, G., Curtis, E., and Longley, J., 2006, "Reducing the Performance Penalty Due to Turbine Inter-Platform Gaps," ASME Paper No. GT2006-90839.

[28] Ranson, W., Thole, K. A., and Cunha, F., 2005, "Adiabatic Effectiveness Measurements and Predictions of Leakage Flows Along a Blade Endwall," ASME J. Turbomach., 127(3), pp. 609-618.

[29] Cardwell, N. D., Sundaram, N., and Thole K. A., 2007, "The Effects of Varying the Combustor-Turbine Gap," ASME. J. Turbomach., 129, pp. 756–764.

[30] Lynch S.P., and Thole K. A, 2011, “The Effect of the Combustor-Turbine Slot and Midpassage Gap on Vane Endwall Heat Transfer,” ASME J. Turbomach., 133(4), 041002.

[31] Piggush, J. D., and Simon, T. W., 2005, “Flow Measurements in a First Stage Nozzle Cascade Having Endwall Contouring, Leakage, and Assembly Features,” ASME Paper No. GT2005-68340.

[32] Piggush, J. D., and Simon, T. W., 2005, “Flow Measurements in a First Stage Nozzle Cascade Having Leakage and Assembly Features: Effects of Endwall Steps and Leakage on Aerodynamic Losses,” ASME Paper No. IMCE2005- 83032.

[33] Chao-Cheng Shiau, Andrew F. Chen, Je-Chin Han, Salam Azad and Ching-Pang Lee, 2016, “Full-Scale Turbine Vane End-Wall Film-Cooling Effectiveness Distribution Using PSP Technique,” ASME J. Turbomach., 138(5), 051002.

[34] Narzary, D. P., Liu K. C., Rallabandi, A. P. and Han, J. C., 2011, "Influence of Coolant Density on Turbine Blade Film-Cooling Using Pressure Sensitive Paint Technique," J. Turbomach., 134(3), pp. 031006-031006.

[35] Chowdhury, N., Dey, P. K. and Ames, F.E., 2011, “The Influence of Inlet Contraction on Vane Aerodynamic Losses and Secondary Flows with Variable Turbulence and Reynolds Number,” ASME Paper No. GT2011-45737.

[36] Chowdhury, M., N., H., K., 2012, “Measurement and analysis of turbulence response near the stagnation region of large diameter cylindrical leading edges with aftbody,” MS Thesis, The University of North Dakota.

[37] Hardy, J. E., McKnight, T. E. and Jones, R. W., 2006, "Automation & Characterization of US Air Force Bench Top Wind Tunnels," Summary Report, Engineering Science & Technology Division, Oak Ridge National Laboratory.

APPENDIX A

HOTWIRE CALIBRATION PROCEDURE

Calibration was required for miniature single wire using in the experiment. A bench top venture type wind tunnel (refer to **Figure 58**) with a throat area of 10cm x 10cm was used to produce the operating range of velocities from 0.50 m/s to 45 m/s. The pressure drop between the inlet and the throat is well correlated with the velocity inside the throat section. The target was set to calibrate hot wire within ± 2 percent that gave an uncertainty of ± 4 percent in the pressure differential according to the Bernoulli's law.

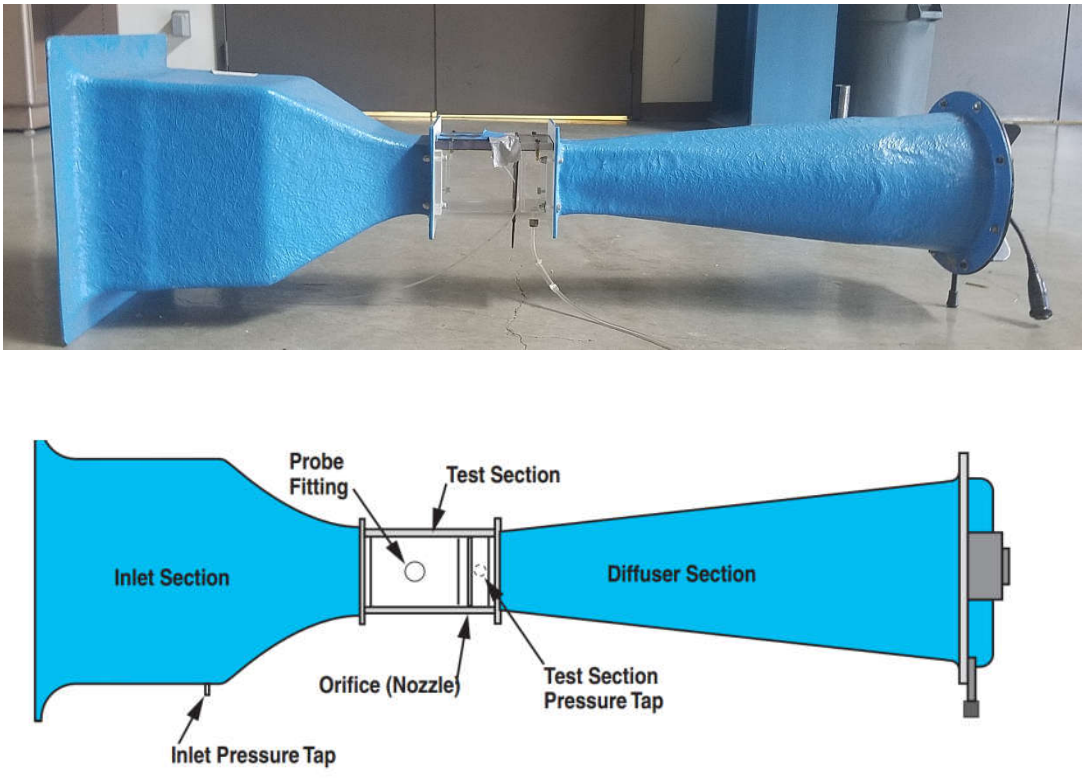

Figure 58 Calibration wind tunnel [37]

It is necessary to use two different nozzle plates (refer to **Figure 59**) to obtain the full band of velocities. These plates are used to control the flow moving through the test section to create slower air velocities. Without any nozzle plate the wind tunnel can produce the range of 7.5 m/s to 45 m/s. The plate with smaller holes (Plate 1) can go from 0.15 m/s to 1.25 m/s where with the larger holed nozzle plate (Plate 2), the range is 1.25 m/s to 7.5 m/s.

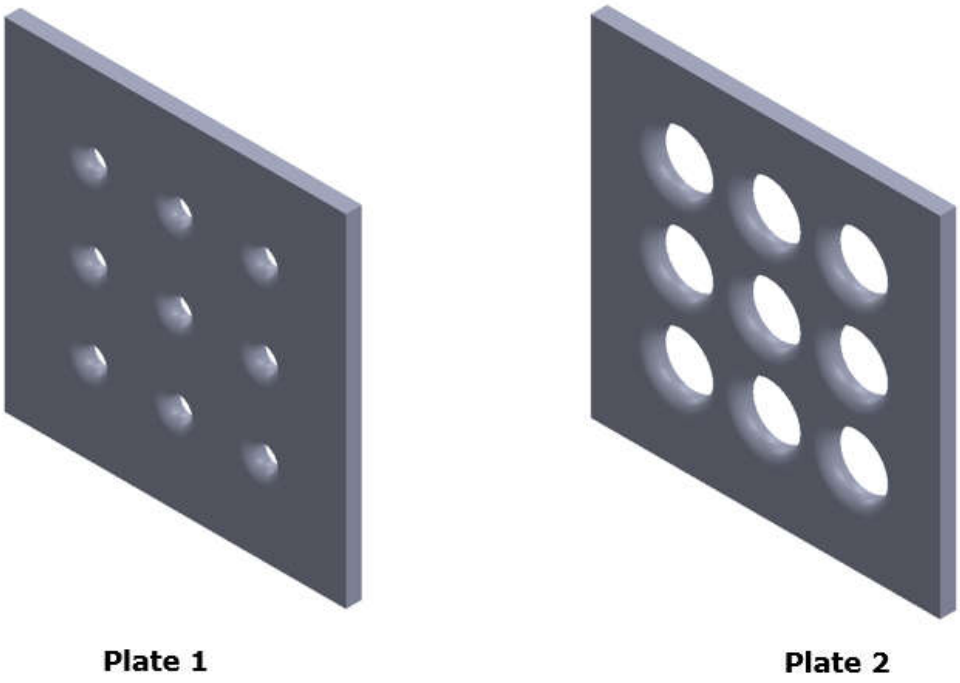

Figure 59 Nozzle plates

Voltage responses produced by the hot wire at different velocities were recorded using calibration program in the StreamWare software. A fourth order regression analysis was performed on the data prior to using the calibration. The regression analysis performed

based on the difference between the measured voltage and the average voltage. The regression fit the data within ± 4 percent for the high velocity range (1.5 m/s to 35 m/s) and within ± 2 percent for the low velocity range (0.5 m/s to 4 m/s). An intended overlap was made in between high and low velocity calibration jets to construct of an entire range of data, from 0.5 m/s to 45 m/s. calibration curve is shown in **Figure 60**.

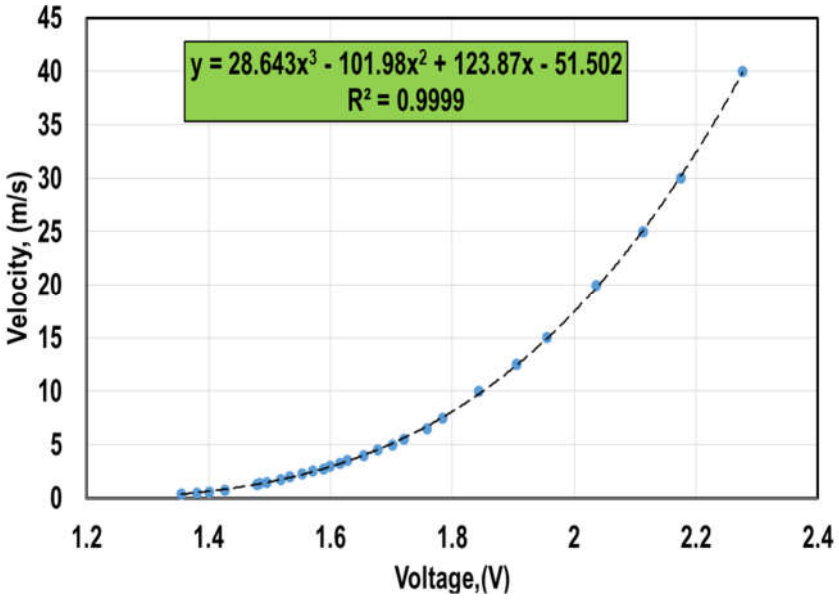

Figure 60 Calibration curve with 4th order polynomial fit

The following procedures should be followed for calibration of a single wire.

1. Choose appropriate wire
2. Calculate the operating resistance using the following equation

$$R_{op} = R_{T/prob} + \alpha R_{20} (T_{sensor/overheat} - T_o)$$

3. Set the operating resistance in the program as calculated.
4. Calibrate the hot wire over the range of velocities.
5. Remove the hot wire and put it away.
6. Shut down the calibration wind-tunnel.
7. Create a single graph of using three velocity ranges.

APPENDIX B

TRAILING EDGE COOLING

Based on the experimental results, two more designs are considered and expected to achieve effectively cooled endwall. The designs are represented in Figure 61 and 62. The arrangements are called mid-chord row and downstream from TE Row.

Mid-chord Row Arrangement

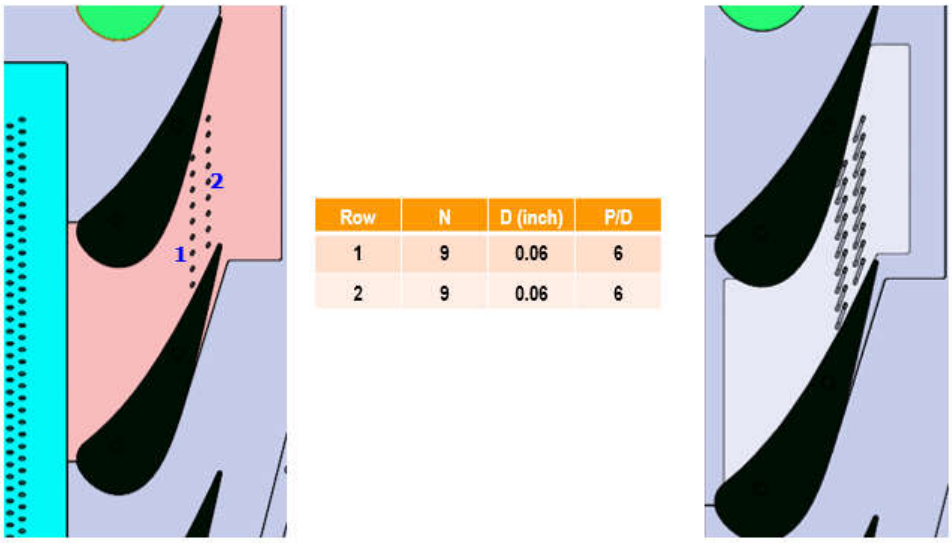

Row	N	D (inch)	P/D
1	9	0.06	6
2	9	0.06	6

Figure 61 Mid-chord row arrangement

Downstream from TE Row Arrangement

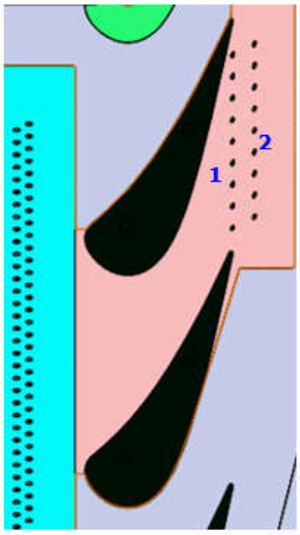

Row	N	D (inch)	P/D
1	9	0.06	8
2	9	0.06	8

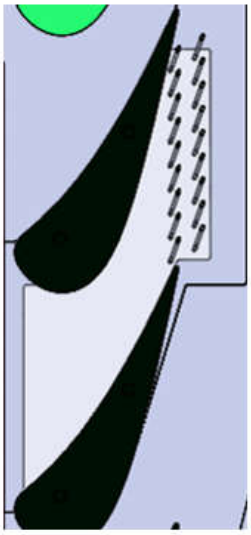

Figure 62 Downstream from TE row arrangement